Wrocław University Of Science And Technology
Faculty Of Electronics, Photonics And Microsystems

Field of study:

Electronics and Telecommunications

Master Thesis

Title Of Thesis:

Silicon sensor characterisation and radiation hardness qualification for the CMS Endcap Calorimeter Upgrade for the High-Luminosity LHC

Autor:

Oliwia Kałuzińska Eng.

Supervisor:

Michał Mazur DSc PhD Eng.

Wrocław 2022

I would like to express my gratitude to dr. Eva Sicking for supervising my one-year technical studentship at CERN and advising me in writing this thesis. Without her support through all the steps of the thesis project, the completion of this study could not be possible.

Contents

List of acronyms

AC – alternating current

ALICE – A Large Ion Collider Experiment

ARRAY – switching mAtRix pRobe cArd sYstem

ATLAS – A Toroidal LHC ApparatuS

CCE – charge collection efficiency

CERN – Conseil Européen pour la Recherche Nucléaire

CE – CMS Endcap Calorimetr

CMS – Compact Muon Solenoid

com. – common (type of p-stop)

CV – capacitance as a function of the bias voltage

CVD – chemical-vapor deposition

DC – direct current

DUT – device under test

ECAL – Electromagnetic Calorimeter

epi – epitaxial

FC – Faraday cage

FZ – float zone

GCD – Gate Controlled Diode

GND – ground

HCAL – Hadronic Calorimeter

HD – high density

HGCAL – High Granularity Calorimeter

HL-LHC – High Luminosity Large Hadron Collider

HPK – Hamamatsu Photonics K.K.

HV – high voltage

ind. – individual (type of p-stop)

IQR – interquartile

IV – leakage current as a function of the bias voltage

IV/CV – current and capacitance probe station

JSI – Jožef Stefan Institute

LD – low density

LGAD – low gain avalanche detector

LHC – Large Hadron Collider

LHCb – Large Hadron Collider beauty

LINAC2 – Linear accelerator 2

LINAC4 – Linear accelerator 4

LL – lower left

LR – lower right

LS – Long Shutdown

MBE – molecular-beam epitaxy

MOS – Metal Oxide Semiconductor

MUXOUT – output multiplexer

MUX512 – multiplexer with 512 channels

NIEL – non-ionising energy loss

PCB – printed circuit board

PS – Proton Synchrotron

RF – radio frequency

RINSC – Rhode Island Nuclear Science Center

SMA – SubMiniature version A (connector)

SPS – Super Proton Synchrotron

TCT – Transient Current Technique

USB – Universal Serial Bus

UL – upper left

UR – upper right

Chapter 1

Introduction

Since the dawn of time, people have wanted to know more about the Universe. Questions such as "What are we made of?" or "Where do we come from?" are timeless. Scientists from all over the world are searching for answers by developing new technologies and use them in experiments. A place that significantly contributes to the development of science is CERN. One of the most important achievements of CERN was the discovery of the Higgs boson at the Large Hadron Collider. The Higgs boson was the final particle predicted in the Standard Model of particle physics, describing the all known elementary particles and three fundamental forces (not including gravitation) of the Universe.

However, there are still many unanswered questions. CERN is upgrading its infrastructure to help find an answer to them. The whole project is called High Luminosity LHC. This thesis is a part of the project, focusing on upgrading the CMS experiment, especially one part – the Endcap Calorimeter. It is presenting the characterisation of the silicon sensors, which is one of the active materials in the upgraded part as well as qualification of their level of radiation tolerance.

Chapter 2 of the thesis is an introduction to CERN and High Luminosity LHC project. It also gives an overview about the CMS experiment and the upgrade of the Endcap Calorimeter. Theoretical aspects about silicon sensors are presented in chapter 3. It describes semiconductors, p-n junctions and the working principle of a silicon based detector. It also provides information about fabrication methods of silicon sensors used for the upgrade project as well as radiation damage that can be introduced in the detector during operation. Chapter 4 presents the prototypes of the sensors and gives details of the samples tested during the time of the thesis work. In chapter 5, the techniques and setups for the silicon sensors characterisation used in this thesis are introduced. Three measurement setups are described in detail. Chapter 6 shows the results obtained during the thesis project. Chapter 7 presents an additional project of integrating two separate setups into one common setup. These two setups are already described in chapter 5. Finally, a summary of the thesis project is presented in chapter 8.

Chapter 2

The CMS Endcap Calorimeter Upgrade

2.1 CERN – introduction

The European Organization for Nuclear Research, also known as CERN, is the world's largest laboratory for experimental and theoretical particle physics. The acronym CERN stands for *Conseil Européen pour la Recherche Nucléaire*. Established in 1954, its main missions is to explore the fundamental structure of the Universe, bring nations together through science and train the scientists by educational programs at many levels. The CERN accelerator complex, presented in figure 2.1, is a great source of knowledge about the fundamental structure of the universe [1]. The experiments performed there, including acceleration and collision of particle beams, allow for a more detailed study of already discovered particles and the identification of new ones. The Standard Model, the theory describing the fundamental particles governed by the fundamental forces, is still incomplete. The theory addresses only three out of the four fundamental forces, omitting gravity. There are also other unanswered questions, for example about the dark matter. The development of the accelerator complex at CERN is aimed at enabling answering these questions and performing new discoveries [3].

Currently, the world's largest and most powerful particle collider is the Large Hadron Collider (LHC). It is where the collisions of the beams are carried out, which are observed in four experiments (detectors): ATLAS, CMS, ALICE and LHCb. The LHC consists of a 27-kilometre ring of superconducting magnets with a number of accelerating structures to boost the energy of the particles along the way. Before the particles reach the Large Hadron Collider, they are initially accelerated in several steps. Protons are accelerated firstly in a linear accelerator – LINAC2, replaced in 2020 by LINAC4, which give them an energy of 160 MeV. The next stage is a so-called Booster, accelerating protons to 2 GeV. Then the protons go to the Proton Synchrotron (PS), where they gain an energy of 26 GeV. The final stage is the Super Proton Synchrotron (SPS), which accelerates the protons to 450 GeV and delivers them to the Large Hadron Collider [4, 5]. All listed accelerators, except LINAC2 and LINAC4, are circular accelerators. Two basic parameters of the accelerator can be distinguished:

- energy of the collision (E),
- luminosity (L).

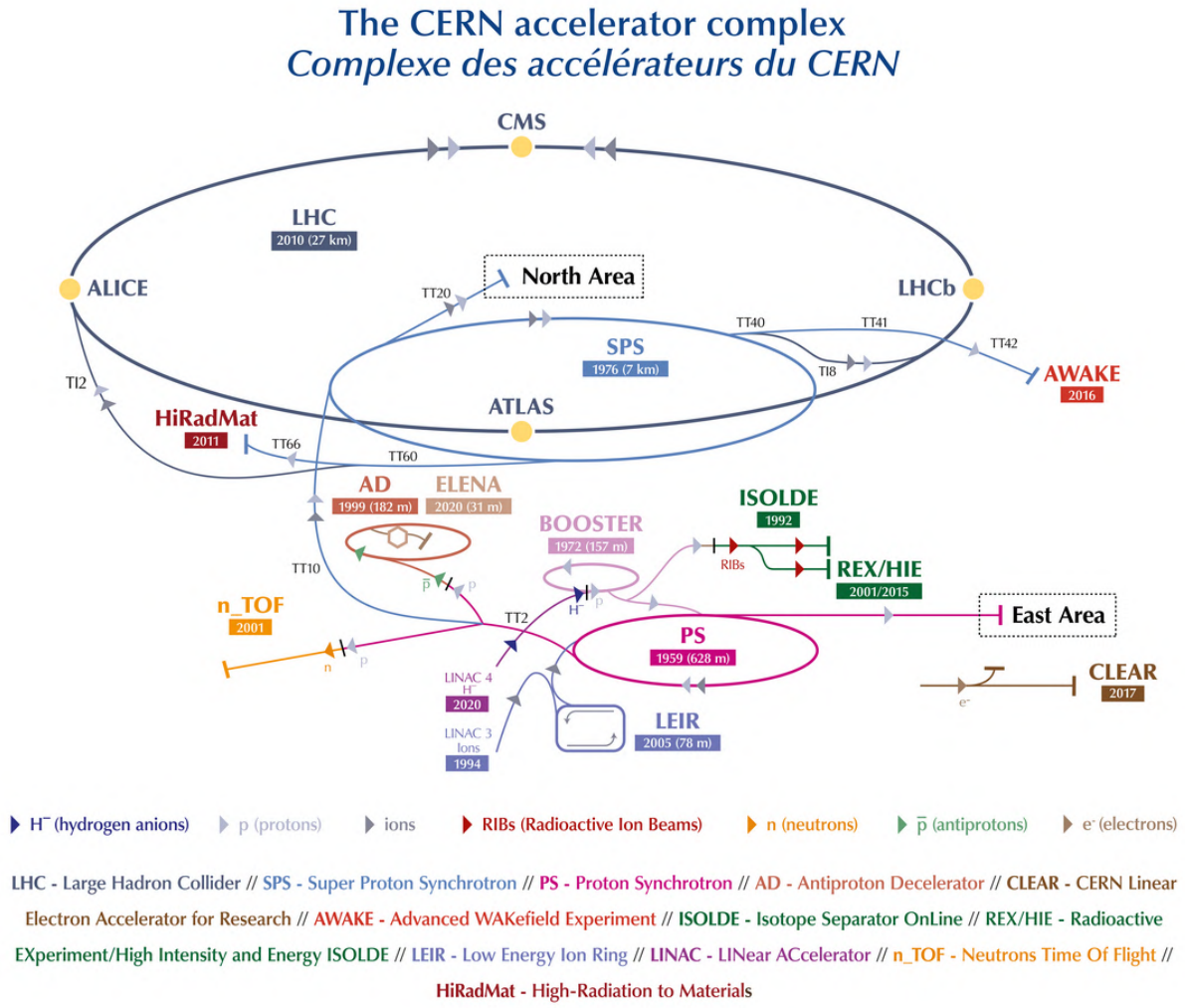

Figure 2.1: A schematic view of the CERN accelerator complex [2].

The instantaneous luminosity is a measurement of the number of collisions (N) per cm^2 and per time unit (dt):

$$L = \frac{1}{\sigma}\frac{dN}{dt} \tag{2.1}$$

In the equation 2.1, σ stands for the cross section. The instantaneous luminosity is expressed in the units of $cm^{-2} \cdot s^{-1}$ or $b^{-1} \cdot s^{-1}$. A barn (b) unit corresponds to 10^{-24} cm^2. The integral of the delivered luminosity over time is called integrated luminosity [6].

2.2 High Luminosity Large Hadron Collider

Currently, CERN is performing an upgrade of the Large Hadron Collider. The project is called the High Luminosity Large Hadron Collider (HL-LHC). The aim of the project is to increase the luminosity of the accelerator, which will increase its efficiency and probability for new discoveries. The upgrade plan is shown in the figure 2.2.

The project is divided into several phases, alternating one after another a so-called Runs, during which the Large Hadron Collider is operating and Long Shutdowns (LS), when the Large Hadron Collider is inactive. During Long Shutdowns, individual parts of

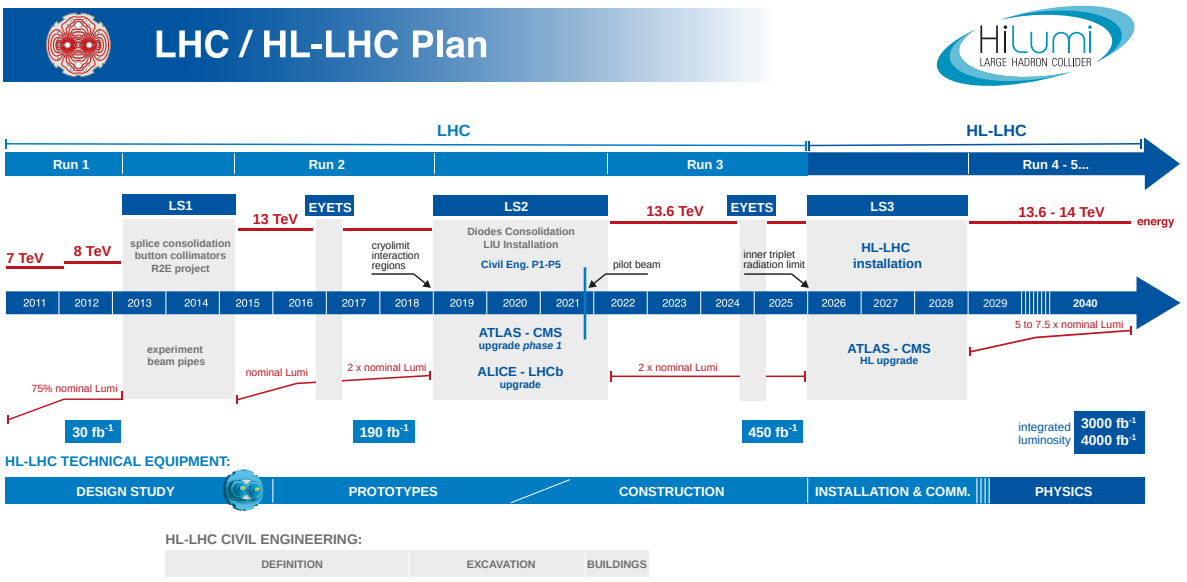

Figure 2.2: The LHC 8 High Luminosity LHC plan [7].

the accelerator are upgraded, while during Runs, the luminosity is gradually increased. In 2029, the instantaneous luminosity is aimed to be even 7.5 times higher than the nominal value ($L = 10^{34} cm^{-2} \cdot s^{-1}$), and the integrated luminosity to be in the range from 3000 fb^{-1} to 4000 $^{-1}$ (currently it is at 190 fb^{-1}) [8].

Successful implementation of the project will enable a more detailed and accurate study of already known mechanisms and particles, such as the Higgs boson, and the observation of rare new phenomena that may emerge. According to the plans, the modernized Large Hadron Collider will produce at least 15 million Higgs bosons annually, compared to about 3 million produced in 2017. This will allow physicists to go beyond the Standard Model, e.g. to study mysterious dark matter. However, the project is very demanding. Major systems such as cooling, vacuum maintenance, particle trajectory control and superconducting electromagnets need to be upgraded. In addition, all four experiments must be adapted to a higher level of radiation (they must be more resistant to the radiation damage) as well as to a larger amount of data [8].

The upgrade of the Large Hadron Collider involves the use of several technologies, some of which are completely innovative. One of them are so-called focusing magnets, generating a 12-tesla magnetic field (compared to 8-tesla for those currently in the LHC). Twelve of them will be installed either side of the ATLAS and CMS experiments. The magnets will better focus the beams before the collision, which will increase the number of collisions and, consequently, the luminosity. The superconducting “crab” cavities will tilt the particle bunches before collision in order to increase the area where they meet by giving them a transverse momentum. As the beams will contain more particles, enhanced machine protection will be required. It relies on collimators – devices that absorb particles that stray from the beam’s trajectory and could otherwise damage the machine. New collimators are being developed, made of a material that produces less electromagnetic interference in the beam and equipped with new instrumentation. About 60 of the 118 existing collimators will be replaced with new collimators and 15 to 20 new ones will

be added. To allow the installation of additional collimators, four 15-metre-long dipole magnets will be replaced with four pairs of shorter magnets (5.5 metres) and four collimators. These new dipole magnets, also referred to as bending magnets, will bend the protons' trajectory by more than 11 metres (instead of 15). Innovative superconducting power lines will connect power converters with new accelerator magnets. These cables are made of the superconducting material of magnesium diboride, which operates at a higher temperature than magnets. They will be able to transfer currents of record intensity, even up to 100 000 amperes. About 80 metres deep shafts were dug near the ATLAS and CMS experiments, as well as two underground 300-metre-long service tunnels. It is intended to house the accelerator equipment that is particularly sensitive to radiation, such as power converters which convert alternating current from the electrical network into high-intensity direct current for the magnets [7, 9].

The High Luminosity Large Hadron Collider is a huge project that requires the upgrade of most systems and all experiments in the accelerator. However, the benefits can be enormous. Thanks to this project, it will be possible to continue research in the field of particle physics and discover new, rare phenomena. This knowledge will allow us to better understand the structure of the Universe and the laws that govern it.

2.3 CMS experiment and Endcap Calorimeter Upgrade

The Compact Muon Solenoid (CMS) is a general-purpose detector – it is designed to observe any new physics phenomena that might occur in the LHC. Its working principle can be explained as a high-speed camera of a giant size, which takes 3D photographs of particle collisions from all directions up to 40 million times each second [10]. The CMS detector is aimed at measuring all stable particles, emerging from the primary interaction process. An "image" of the collision can be recreated by identifying and measuring momentum and energy of these particles. The name of the detector comes from the three features: it is relatively compact (C), compared to ATLAS – a detector of similar purpose. The CMS detector is 21.6 metres long and has a diameter of 14.6 metres and its total weight is of 14 000 tons [11]. It is designed to detect particles known as muons (M) very accurately and at its heart a large superconducting solenoid (S), producing magnetic field of nearly 4T, is placed [10, 11]. Figure 2.3 shows a cross section of the experiment.

The detector consists of several layers, each dedicated for a different task. The innermost part of the experiment is the tracking system made of silicon-pixel and silicon-strip detectors. They are located around the interaction point and enable tracing the trajectories of the charged particles and determine their momenta. Two other layers are the Electromagnetic Calorimeter (ECAL) and the Hadronic Calorimeter (HCAL). A calorimeter in particle physics is a dense detector that completely absorbs a particle to be measured and the energy absorbed transform into a measurable quantity [12]. The ECAL surrounds the tracking system and is designed to measure particles such as photons and electrons. The HCAL is design to detect hadrons such as protons, neutrons and pions [13]. The tracking system and the calorimeters are placed inside the solenoid magnet, which is formed by a cylindrical coil of superconducting cables. The magnetic field bends the trajectories of the charged particles to identify the charge of the particle and to measure the momentum of the particle. It is the heaviest component of the CMS detector, as it

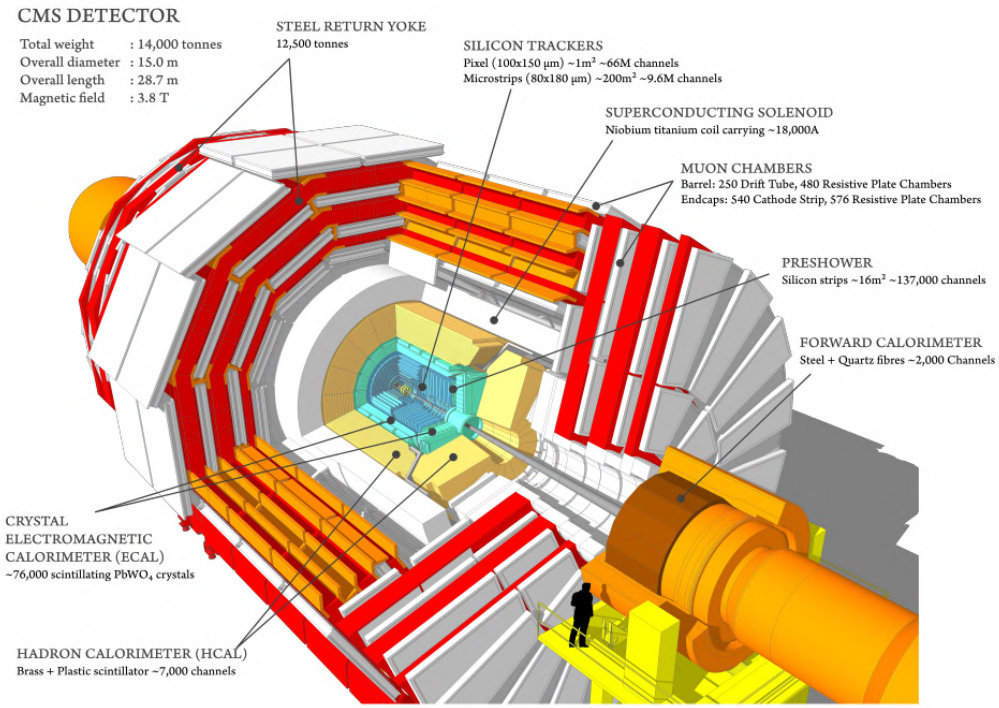

Figure 2.3: The CMS detector overview [10].

weighs 12 500 tons. The high magnetic field that is produced there is then returned by a so-called steel return yoke, which is divided in three layers and interspersed with the muon chambers. Muons belongs to lepton group, similarly as electrons, but are around 200 times heavier. They traverse through the CMS sub-detectors including the muon chambers, the outermost part of the CMS detector [10, 14].

As mentioned in the section 2.2, the CMS is one of the four experiments to be uprgaded for the High Luminosity LHC. The present thesis focuses on one aspect of the CMS detector upgrade, namely the Endcap Calorimeter. It consists of the fragment of the electromagnetic and hadronic calorimeter, as shown in figure 2.4.

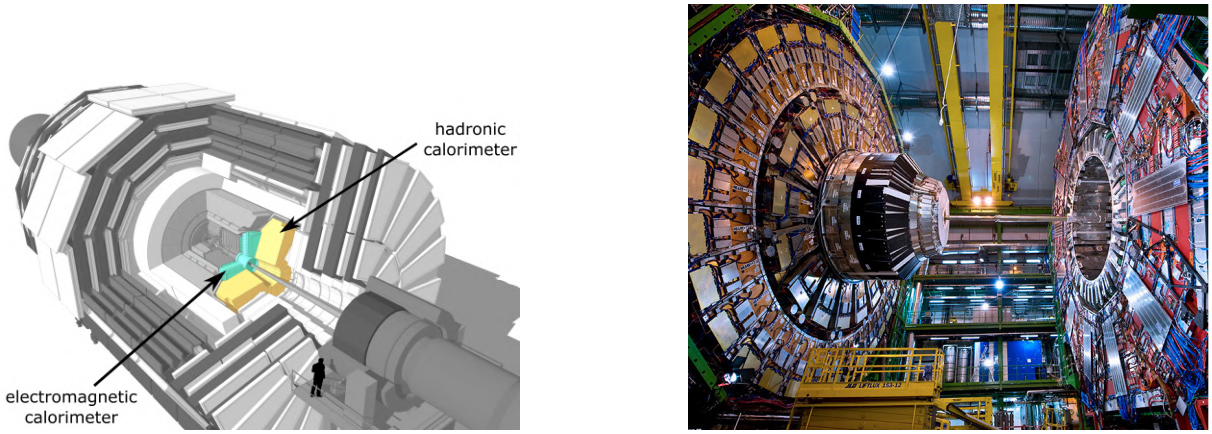

(a) (b)

Figure 2.4: The current Endcap Calorimeter: a) location within CMS detector [15] and b) picture of this part [16].

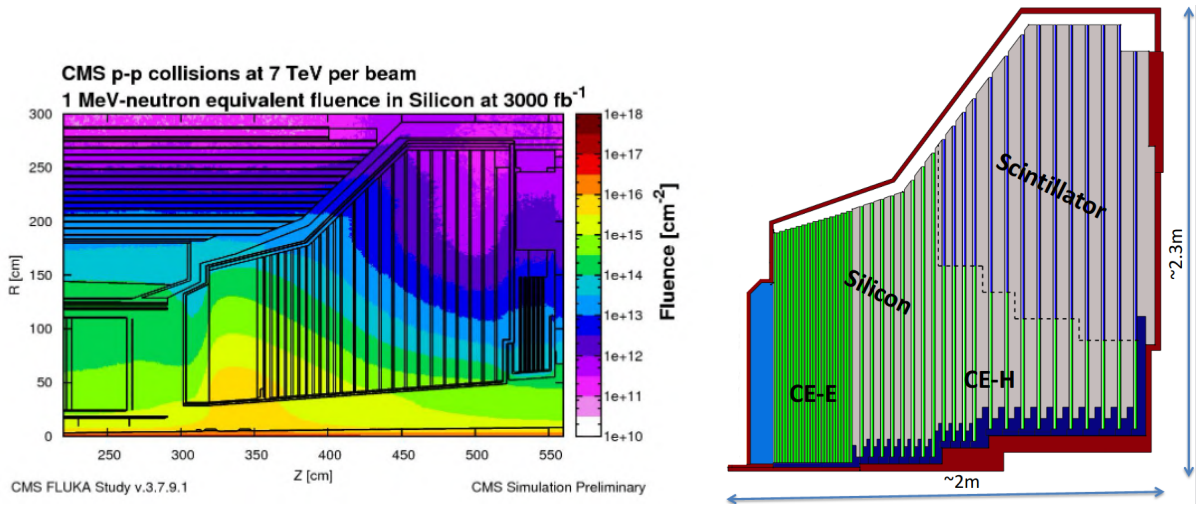

(a) (b)

Figure 2.5: HGCAL: a) expected fluences across the new calorimeter [17] and b) cross section of the new calorimeter design [18].

The CMS Collaboration proposed to replace the Endcap Calorimeter by a new, upgraded calorimeter, referred to as High Granularity Calorimeter (HGCAL). The project is also referred to as the CMS Endcap Calorimeter (CE) Upgrade. HGCAL is a sampling calorimeter, which has alternating layers of passive absorber (e.g. Pb, Cu) and active detector layers (e.g. Si). The passive absorber produces the particle shower, whereas the active layers sample the shower energy between the passive layers and measure it. The new calorimeter will provide high lateral and longitudinal granularity to obtain high signal-to-noise ratio and ensure good energy resolution. Moreover, HGCAL will offer good time resolution. It is important due to increased *pile-up* – additional inelastic number of collisions per bunch crossing. Pile-up creates significant activity in the detector and has to be rejected [14].

HGCAL has to be resistant to much higher radiation levels, even ten times higher than in the original CMS design [17]. The results of the simulations (shown in figure 2.5a), point out that at the luminosity of 3000 fb^{-1} fluences up to 10^{16} 1-MeV-neutron-equivalents per square centimeter (n_{eq}/cm^2) can be expected. Such level of radiation will be seen near the symmetry axis of the cross section of the HGCAL, which is close to the beam pipe (cf. fig. 2.5a). An overview of the most recent HGCAL design is shown in figure 2.5b. In the high radiation regions the HGCAL will be based on silicon as active material. It is the entire electromagnetic calorimeter (CE-E) and the inner part of the hadronic calorimeter (CE-H). The outer part of the hadronic calorimeter, where lowest radiation levels are expected, will be based on scintillators coupled to silicon photomultipliers. The total area of the silicon sensors in the HGCAL will be around 620 m^2 and the total number of channels will be around 6 million. The details on the silicon sensor layout is presented in the section 4.1. The silicon sensors will be placed in a so-called modules. A module is a stack of four components: baseplate, Kapton-gold sheet, silicon sensor and the printed circuit board (PCB) [17]. The silicon modules will be grouped together creating a sandwich structure referred to as cassettes [14].

Chapter 3

Silicon sensors in High-Energy Physics

3.1 Working principle

Position sensitive semiconductor devices were developed for the detection and characterisation of charged particles and are nowadays widely used in experimental particle physics. They exhibit several unique properties that are desirable for high-energy physics, for example: ability of extremely precise position measurement, high readout speed, the simultaneous measurement of energy, position and arrival time and the possibility of integrating detector and readout electronics on a common substrate [19]. Important for the application in HGCAL are especially the energy measurement and the timing measurement. The semiconductor material that is most widely used in high-energy physics is silicon. In the following section the working principle of the silicon-based detectors is described.

Solid state materials can be divided into three groups: insulators, semiconductors and metals. They are defined by the arrangement of the energy bands – the valence band and the conduction band. The energy band diagrams for each group are shown in figure 3.1. In metals, the valence and the conduction band overlap, whereas in semiconductor and insulators, the energy bands are separated by the bandgap. The bandgap energy, the forbidden energy gap, is the energy range between the bottom of the conduction band and the top of the valence band [20].

Semiconductors are materials with small energy gap, on the order of a few eV. At absolute zero temperature ($T = 0$ K) and in the absence of impurities, all electrons are in the valence band and there are no electrons in the conduction band thus conduction is impossible. At room temperature however, electrons can be thermally excited from the valence band to the conduction band where they become free current carriers. At the same time, holes are formed in the valence band, which can act as charge carriers, too [20].

Silicon, a semiconductor material, belongs to group IV of the periodic table. At room temperature, the bandgap energy of this element is 1.12 eV [20]. In the absence of impurities, the concentration of electrons n in the conduction band and the holes p in the valence band are equal: $n = p = n_i$. A semiconductor with such property is called *intrinsic*. To estimate the number of free charge carriers in equilibrium (i.e. the steady-state condition at a given temperature with no external excitations), the Fermi-Dirac function [20] can be used:

$$F(E) = \frac{1}{1 + exp(\frac{E - E_F}{kT})} \tag{3.1}$$

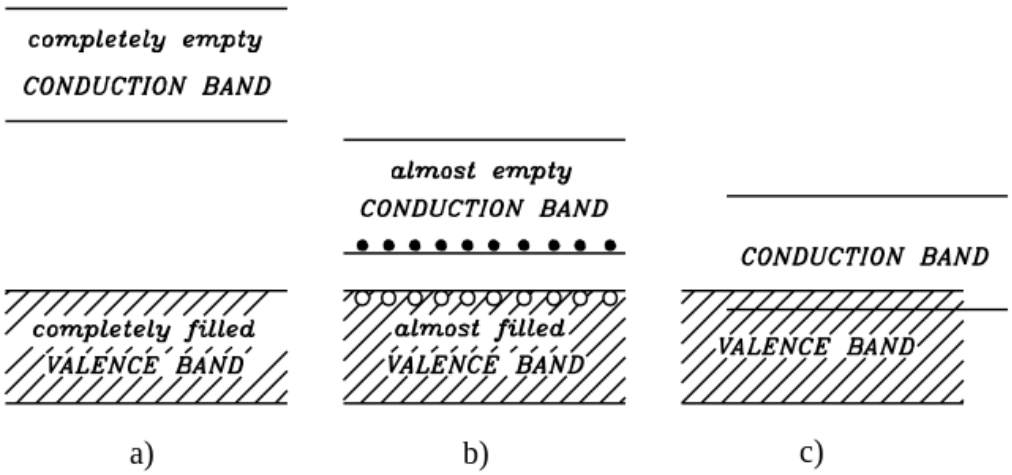

Figure 3.1: Energy band structure of: a) insulators, b) semiconductors, c) metals [19].

Equation 3.1 expresses the occupation probability for an electronic state, where E_F is the Fermi energy (the energy at which the probability of occupying a state is 0.5), k is the Boltzmann constant and T is the absolute temperature. In order to enhance the conductivity of the intrinsic silicon, additional states in the forbidden gap can be inserted. The process is called *doping*. Silicon can be doped in two ways: by adding group V element (e.g. arsenic or phosphorus) and thus creating *n-type* silicon with additional electrons or by adding group III element (e.g. boron) and thus creating *p-type* silicon with additional holes [19–21].

The structure that performs a significant function in modern electronics applications is a p-n junction (or diode). It is formed by connecting p-type and n-type materials. When these two regions are brought into contact, electrons will diffuse from the n-side into the p-side and holes from the p-side to the n-side. As a result, a surplus of negative electric charge in the p region and of positive charge in the n region will be created. This generates an electric field that induces a drift counteracting the diffusion [20]. In thermal equilibrium and without external voltage applied, diffusion and drift stabilize and a region depleted from freely moving charge carriers is formed around the boundary of p- and n-sides. The region is called *depletion region* or *space-charge region*. Figure 3.2a shows a p-n junction and corresponding energy band diagram in equilibrium. The Fermi levels must line up resulting in bending the energy bands across the p-n junction. The resulting potential difference is referred to as the *built-in voltage* (V_{bi}), defined as [19]:

$$V_{bi} = \frac{1}{q}(E_i^p - E_i^n) = \frac{kT}{q} ln \frac{N_A N_D}{n_i^2} \tag{3.2}$$

In equation 3.2, E_i^p and E_i^n denote intrinsic levels on the neutral p and n regions, respectively, N_A denotes the acceptor concentration and N_D is the donor concentration. The width of the depletion region is given by [19]:

$$W = \sqrt{\frac{2\epsilon\epsilon_0(N_A + N_D)}{qN_A N_D} V_{bi}} \tag{3.3}$$

In equation 3.3, ϵ_0 and ϵ denote the vacuum permittivity and the relative material permittivity, respectively. The depletion region width depends on the doping concentrations of p- and n-type materials.

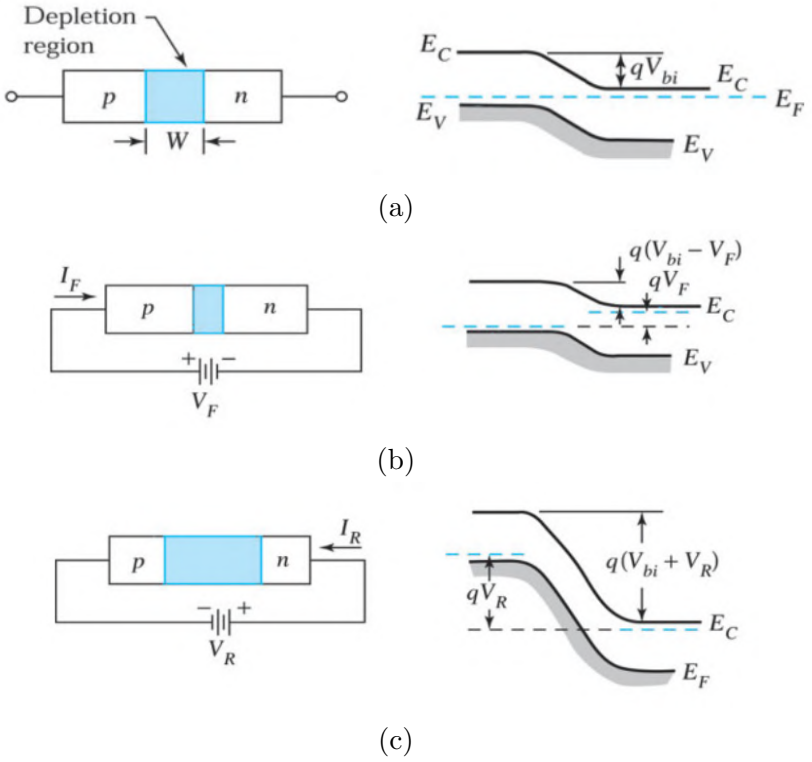

Figure 3.2: Depletion region of the p-n junction and its energy band diagram presentation for three cases: a) no external bias voltage applied, b) forward biased, c) reverse biased [20].

The p-n junction can be biased in two ways. If an external positive voltage V_F is applied to the p-side and negative to n-side, the p-n junction is forward biased. This situation is shown in figure 3.2b. The built-in voltage decreases to $V_{bi} - V_F$, resulting in decreasing the width of the depletion region. In contrast, if an external negative voltage is applied to the p-side and positive to n-side, the p-n junction is reverse biased, as shown in figure 3.2c. The built-in voltage increases by V_R, that is, it is equal to $V_{bi} + V_R$. In this case the depletion region width is enlarged [13, 19, 20].

The p-n junction can only conduct the current when it is forward biased. However, under reverse bias, some current flows through the depletion region. This current is referred to as *leakage current*. It is caused by diffusion of the minority carrier across the depletion region and carrier generation within the depletion region. Irradiation of silicon diodes leads to generation of defects in the silicon bulk. The defects conduce to thermal generation of electron-hole pairs resulting in significant rise in the leakage current, which can affect the sensor performance. It contributes to the noise of the detector which impacts the position resolution [13, 22]. The effects of irradiation are described in the section 3.3.

The p-n junction can be transformed into a position sensitive detector by segmenting the front side implant, i.e. creating multiple front side implants instead of one big implant. The readout of the signal is done from all implants separately. A charged particle can traverse the sensor based on p-n junction with segmented implants and generates electron-hole pairs. Charge carriers that are created in the depletion region are collected by the electrodes while the charge produced outside this region is lost due to recombination with

free carriers. That is why the silicon sensors are operated under the full depletion, that is, when the reverse bias voltage is high enough that the depletion region extends over the full width of the p-n junction. The minimum value of the reverse voltage at which the junction is fully depleted is called *full depletion voltage* [13].

3.2 Silicon-sensor fabrication methods used for HGCAL

For a silicon to become a position sensitive sensor to be used in HGCAL, it has to undergo a series of manufacturing processes which are described in the following section. The single crystal for the HGCAL applications is produced from polycrystalline silicon using two methods – float zone and epitaxial growth.

In the float zone process, a polysilicon rod is contacted to a seed crystal at the bottom, held in a vertical position and rotated. A small zone of the crystal is melted with radio-frequency (RF) heating. The heater is moved along the rod and this *floating zone* passes through the entire rod. Surface tension between the melting and growing faces holds the molten silicon. When the floating zone moves up, a monocrystalline silicon freezes at the zone's retreating end and grows as an extension of the seed crystal. The ingot is then cut into wafers [20]. The float zone method is shown in figure 3.3a.

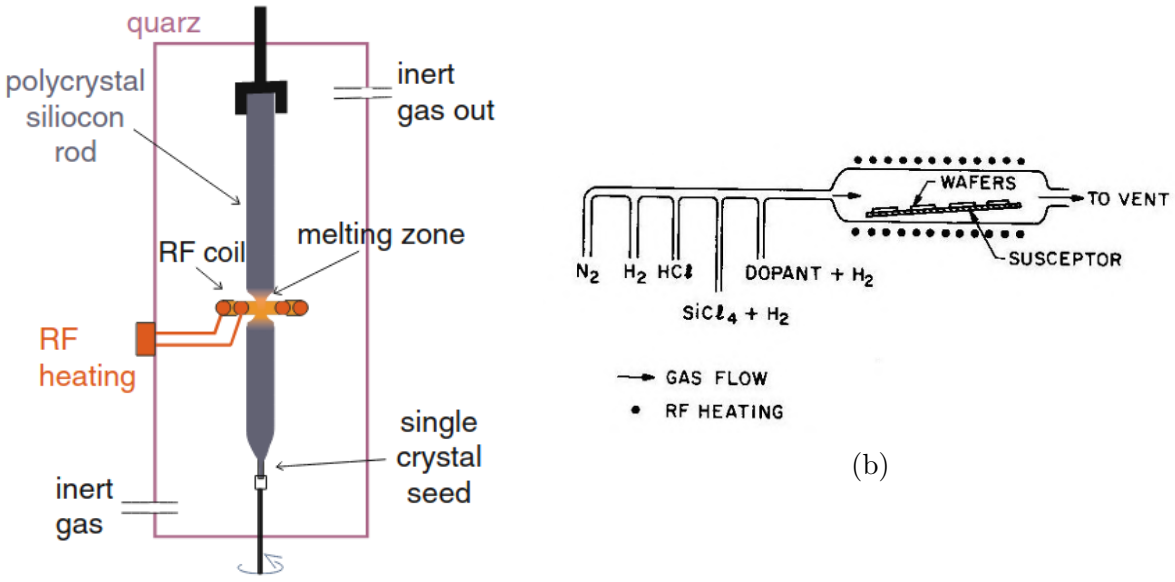

(a) (b)

Figure 3.3: Silicon fabrication methods for HGCAL: a) float zone [21] and b) example of epitaxial growth (CVD) [23].

Epitaxial growth is a different method of silicon fabrication, where a substrate wafer acts as the seed crystal and the process is performed at lower temperatures. There are two common techniques for the epitaxial growth: chemical-vapor deposition (CVD) and molecular-beam epitaxy (MBE) [20].

In the CVD method, shown in figure 3.3b, a chemical reaction between gaseous compounds forms an epitaxial layer on a substrate. The process can be performed at atmospheric or low pressure. Silicon is grown from different sources, the most common is silicon tetrachloride ($SiCl_4$). The reactants (gases and dopants) are delivered to the

substrate area and are adsorbed on a substrate surface. Then, a chemical reaction takes place ending with the growth of an epitaxial layer [20].

MBE is a deposition process, where one or more thermal beams of atoms reacts with the wafer surface. The process is performed under ultrahigh-vacuum conditions. MBE growth is slow ($\sim$ 1 µm/h [20]) but the control of the process is very precise. The method allows to product structures with dimension in the order of atomic layers [20].

The next step of manufacturing process after wafer production is bulk doping to create n- and p-type silicon. It can be done in two ways, namely thermal diffusion and ion implantation [20]. In the diffusion method, the dopants are placed on the wafer by deposition from the gas phase. The ion implantation consists in doping the material by means of an ion beam [20]. Very often both processes are employed in the fabrication of microelectronic devices as they are generally complementary to each other. After doping process, the structure is annealed at high temperatures to remove defects, activate the dopants and re-establish essential parameters of the material [13, 20].

The structure undergo also a front side processing. This includes several steps, the first one is oxidizing the wafer. Then, the aluminium metallization of the full surface by a CVD sputtering is performed. The next step is lithography and etching, in which aluminium strips are created. The last part is the passivation of the front side. The back side is fully metallized to provide an electrical contact [21].

3.3 Radiation damage of the bulk material

As mentioned in the section 2.3, the HGCAL silicon sensors will be exposed to high fluences (up to 10^{16} n_{eq}/cm^2) resulting in generating bulk damage in the sensor. Radiation can dislocate lattice atoms and create point defects in the silicon bulk. The dislocated atom is called interstitial and in its place a vacancy is left. This pair is also known as *Frenkel pair*. The particles responsible for creating such defects are mainly heavy particles such as neutrons or protons. As a consequence, additional energy levels in the bandgap are generated [21]. The radiation damage produced by incident particles can be quantified and scaled by the so-called *non-ionising energy loss (NIEL) hypothesis*. The NIEL hypothesis assumes that the amount of radiation damage due to lattice displacements produced in the material is linear proportional to the non-ionizing energy loss of the traversing particles. Therefore, the damage caused by different particles can be scaled with the use of the NIEL hypothesis [22].

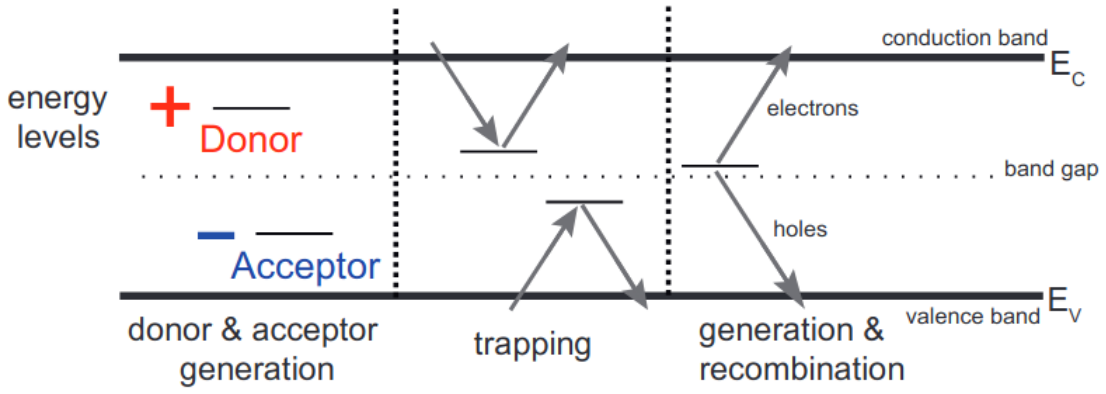

Figure 3.4: Different effect of radiation induced defects [24].

Shallow defects located close to the boundaries of the bandgap act as donors and acceptors and change the effective doping concentration. Free charge carriers can be trapped in the levels located close to the center of the bandgap, what leads to decrease in the efficiency of the charge collection. The defect can also cause the change of the charge density in the depletion region, resulting in the increase of the full depletion voltage. These effects can be limited by decreasing the temperature at which the sensor is operated. However, there is another consequence of the radiation damage. The additional levels created in the bandgap also act as centers for electron-hole pairs generation and recombination processes in the depletion region. They cause increase in the leakage current. The change of the leakage current (ΔI) per bulk volume (V) scales linearly with fluence (ϕ) [22]:

$$\Delta I = \alpha \cdot \phi \cdot V \tag{3.4}$$

The proportionality factor α is referred to as *current related damage rate* [14, 19]. All mentioned effects of the radiation induced defects are shown in figure 3.4. The level of the leakage current as well as alpha value are studied in this thesis for the test structures of different thicknesses and exposed to different fluences. Moreover, isothermal annealing studies on the samples are performed to observe the effect of the thermal annealing. In high temperatures (T $>$ 150K), interstitials and vacancies are very mobile. As a result, several effects of the defects diffusion can be observed, such as: Frenkel pair recombination, interstitial and vacancy combination and complex defects combination. The annealing has a beneficial part where the damage is reduced and a reverse part where the electrical properties of the sensor degrade [21, 22]. The electrical characterisation of the test structures presented in this thesis includes an annealing study. The samples are annealed in several steps to reach the reverse part and to be able to determine the end of the beneficial part.

Chapter 4

Silicon sensor prototypes for HGCAL

4.1 Wafer layout and components

The silicon sensors for the CMS High Granularity Calorimeter are produced in hexagonal geometry diced from 8-inch circular wafers. The hexagonal shape is the most efficient way to use the wafer area, compared to square or rectangular geometries. The corners (vertices) of the hexagon are truncated, what allows clearance for the mounting and fixation system and also increases the wafer surface usage [17]. Each sensor is segmented into several hundred diodes also known as cells (or channels, pads) of mainly hexagonal (standard) shape.

For the CMS Endcap Calorimeter Upgrade diodes with p-type bulk ("n-in-p") were chosen, as they show better radiation hardness and noise performance than n-type devices [15]. The sensors are produced in three active thicknesses, that is 300 µm, 200 µm and 120 µm. The cross sections of each diode are shown in figure 4.1. The 300 and 200 µm sensors are fabricated using the float zone method made from 600 µm wafers which are thinned to target thickness on the backside after front side processing. Then, a so-called field-stop implant is introduced at the wafer backside, which is very thin (around 1 µm) and makes these diodes very sensitive to backside scratches. The 120 µm sensors are produced in the epitaxial process. They have thick substrate wafer (around 200 µm), on which the epitaxial wafer is grown.

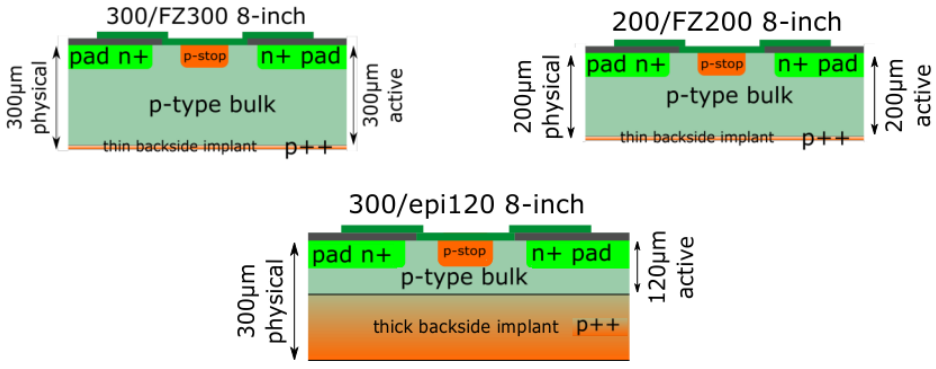

Figure 4.1: Sensors cross section (not to scale): 300, 200 and 120 µm; FZ denotes float zone process and epi – epitaxial process [15].

The sensor electrodes are inserted at the upper part of the p-type bulk and are denoted as n+ implants (or n+ pads). They have to be isolated from each other to provide precise position resolution. It is achieved by introducing a so-called *p-stop* implant in-between. This is shown in figure 4.1. For the HGCAL, two different p-stop layouts are considered in the prototyping phase: a so-called *individual p-stop* version, where each cell is surrounded by an individual p-stop ring and a larger ring separates the cells and a second version referred to as *common p-stop*, where the individual cells and the inner guard ring are separated by a common p-stop grid [13].

On the top of the p-type bulk, metal contacts are located to provide signal readout. A thin layer of high quality silicon dioxide (SiO_2) is inserted between the n+ pad and metal contact and acts as the coupling dielectric. In the present thesis, oxide layers are produced with different processes (called oxide types). Basic oxide type is a so-called standard type (STD) with -2 V of flatband voltage V_{fb} (in MOS capacitors: voltage at which the energy bands are flat) [13].

A top side of the sensor is covered by a passivation layer, to protect it from environmental influences and damage and to electrically isolate the front side of the sensor. The most common material used for passivation is silicon dioxide SiO_2 [13].

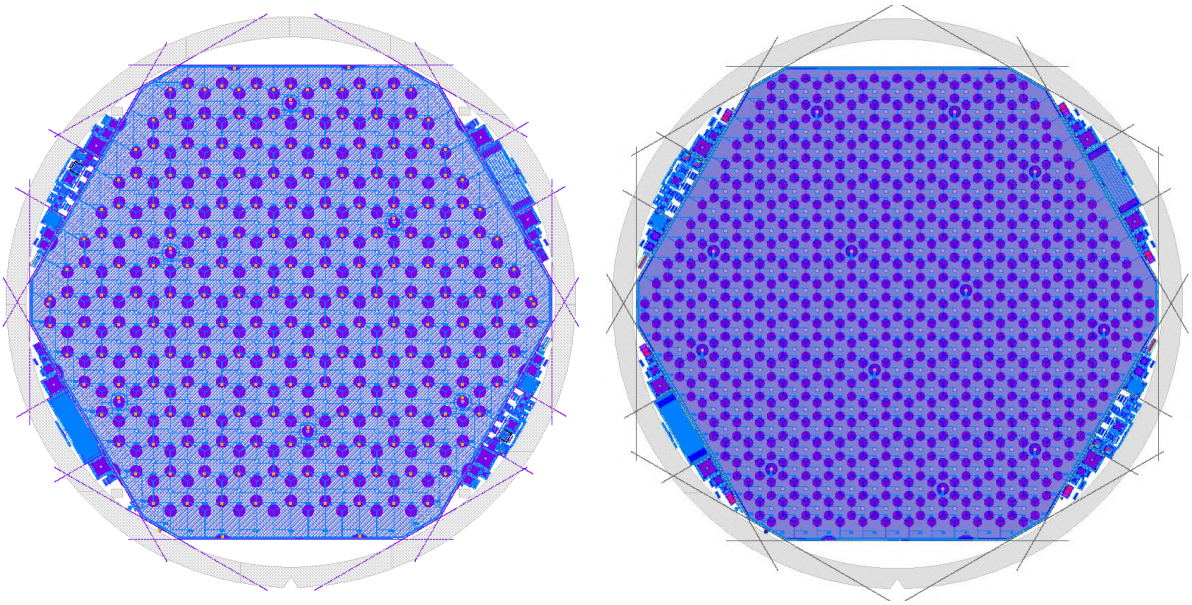

(a) (b)

Figure 4.2: Sensor designs for HGCAL: (a) low and (b) high density layout. Both wafer layouts include the main hexagonal sensor and four halfmoons containing test structures [25].

On the full sensor the cells are numbered. There are a few cells with different geometry – the so-called "calibration cells" and edge cells. Depending on the thickness of the sensors, there are two types of the layout defining the number of the cells: low density (LD) and high density (HD). The two layouts are shown in figure 4.2. The low density sensors have 198 channels, from which 141 are of standard geometry (1.1 cm^2 size). They are produced in thicknesses of 300 µm and 200 µm in the float zone process. The high density sensors have 444 channels and 351 of them are standard cells (0.5 cm^2 size). They are produced only in 120 µm thickness in epitaxial process [17]. In this work only low density full sensors are studied. The special cells of the LD sensor are visible in figure 4.3 and 4.4:

- calibration cells:
  - inner calibration cells (e.g. 14, 62),
  - outer calibration cells (e.g. 13, 61),
- edge cells:
  - corner cells (e.g. 1),
  - mouse bits cells (e.g. 9),
  - small half cells (e.g. 2),
  - small half cells with cut out (e.g. 3),
  - big half cells (e.g. 39),
  - big half cells with cut out (e.g. 28).

A channel map of the low density sensor with cell numbers is shown in figure 4.3. The full sensor has also a guard ring (numbered as cell 199) which surrounds all cells to protect from dark currents originating at the sensor's dicing line [15, 17].

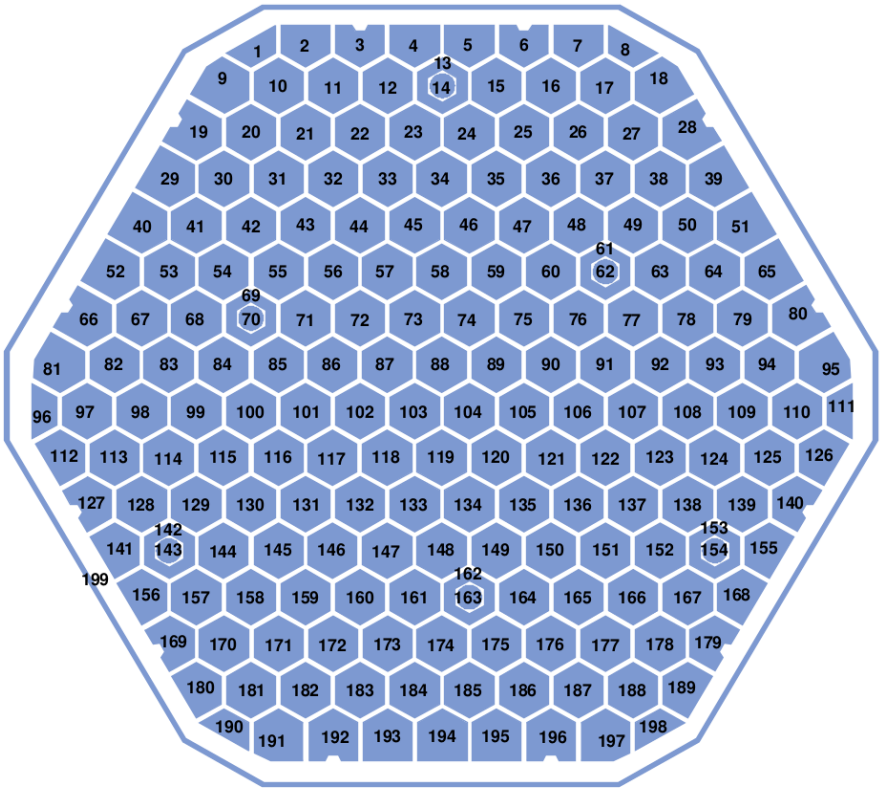

Figure 4.3: Channel map of the low density sensor [26].

When the full hexagonal sensor is diced from the circular wafer, remaining pieces are not wasted. On four pieces (called also "halfmoons"), visible in fig. 4.2 in the corners, small test structures are produced. Detailed pictures of all halfmoons are presented in figure 4.5.

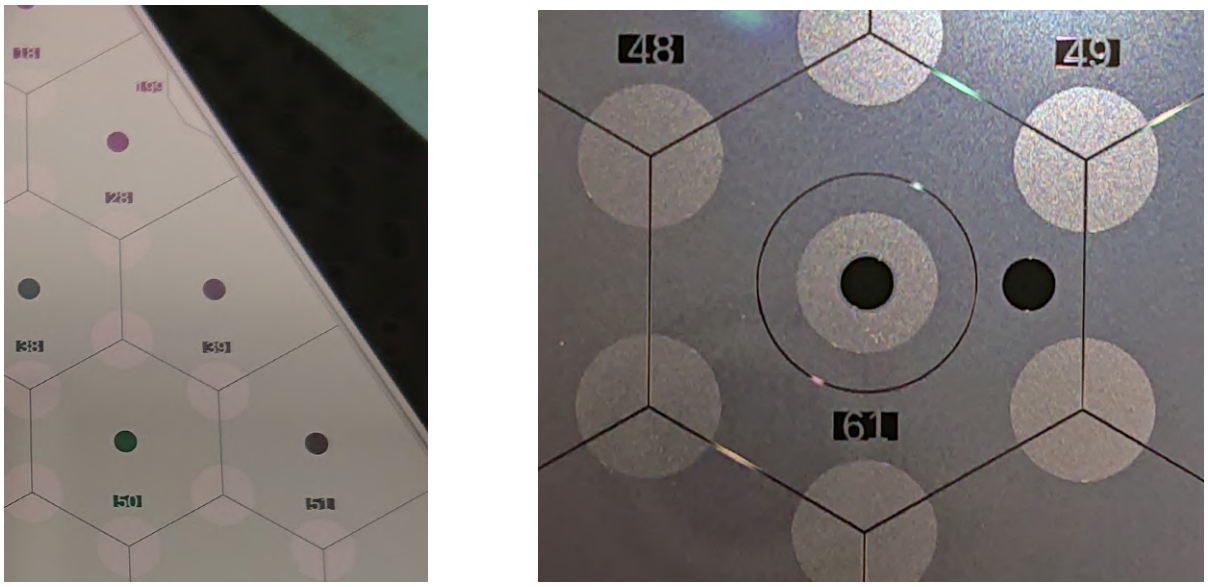

(a) (b)

Figure 4.4: Enlarged pictures of a) edge cells, b) inner and outer calibration cell of a HGCAL low density sensor.

The halfmoons are distinguished by their position on a wafer – they are described as: upper left (UL), upper right (UR), lower left (LL), lower right (LR), respectively. Each halfmoon contains many test structures, such as single diodes (the same structures as a cell on a full sensor), MOS (Metal Oxide Semiconductor) capacitors and GCDs (Gate Controlled Diodes) used for determination of oxide layer quality and mini strip sensors. Thanks to their small size, they can be easily measured instead of the full sensors, using infrastructure which is not adapted for full wafers. For example, the charge collection property (cf. sec. 5.1.2) is only measured on the single diodes (using the existing setup for small devices). A setup for measuring the charge collection of the full 8-inch sensor is under construction up to the time of the thesis project. The behaviour of the test structures is assumed to be the same as of the full sensors. In this work only single diodes are studied from the test structures group. All the devices introduced in this work are produced by an external company – Hamamatsu Photonics K.K. (HPK) [15].

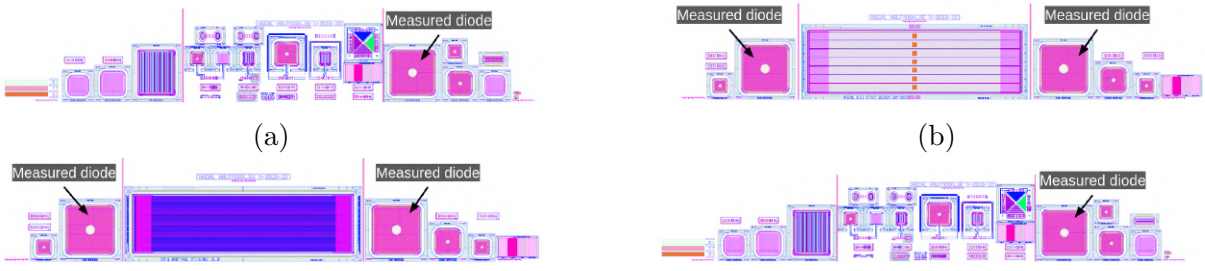

(a) (b)

(c) (d)

Figure 4.5: Halfmoons: a) upper left, b) upper right, c) lower left, d) lower right. The arrows point to the diodes used in this thesis [27].

When the full 8-inch circular wafer is produced, the halfmoons and other parts have to be separated from the full sensor. To this end, the whole structure is mounted on

a so-called dicing frame, which has a sticky surface that holds the wafer, surrounded by a plastic frame. Then, dicing of individual components can be performed. In the process of removing the structure from the dicing frame, separated parts are obtained. An example of a full wafer on a dicing frame is shown in figure 4.6.

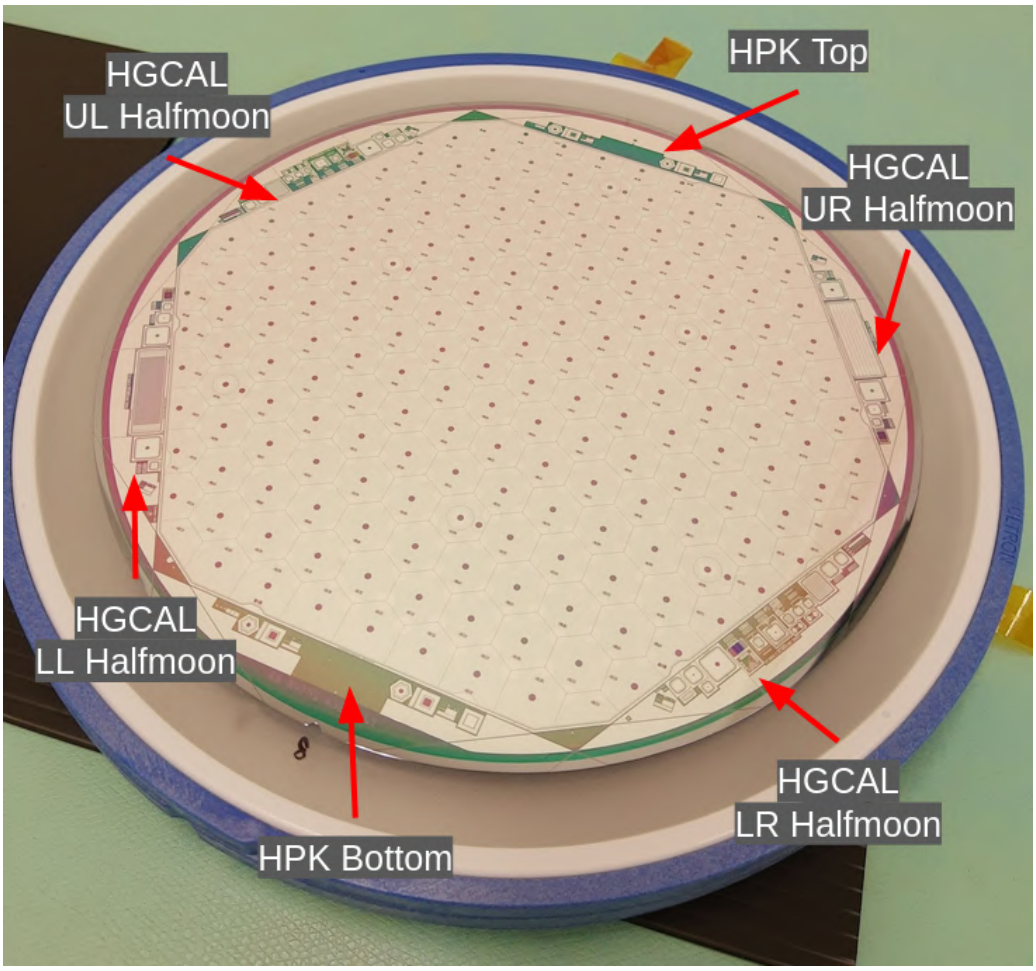

Figure 4.6: HGCAL low density sensor on a dicing frame. One can see the four HGCAL halfmoons, as well as two halfmoons designed and used by the sensor producer (HPK).

4.2 Neutron irradiation of the structures

In order to simulate the sensor's damage in real conditions inside the CMS detector when the LHC is running, the structures are subjected to neutron radiation of different fluences. As the thinnest sensors will be placed in the highest radiation regions, they are exposed to the highest fluences, up to 10^{16} n_{eq}/cm^2. For the irradiation of the samples presented in this thesis, two facilities were used.

The first one is Jožef Stefan Institute (JSI) in Ljubljana (Slovenia). It has a pool type nuclear reactor TRIGA Mark II constructed to provide neutrons for experimental purposes, which can be run with a large span in operating power (few W to 250 kW), enabling irradiations with various neutron fluxes at the same irradiation site. About 1/3 of the flux is composed of fast neutrons (above 0.1 MeV) [28]. The reactor has the following experimental and irradiation facilities: two radial beam ports, two tangential

beam ports, two thermal columns, 40 position rotary specimen rack, pneumatic transfer tube, central thimble and extra irradiation position in F ring [29]. The main part of the reactor is its core, consisting of fuel and control rods. The reactor core is surrounded by a graphite reflector and placed into a reactor vessel filled with water, all within a thick concrete shield. A schematic view of the reactor cross-section is shown in figure 4.7.

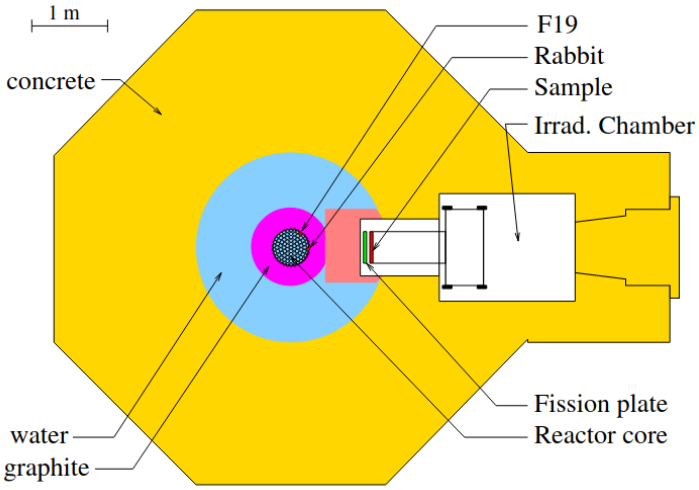

Figure 4.7: Schematic view of the reactor cross-section [28].

In general, irradiation sites can be divided into two groups. Vertical channels occupying a fuel rod position give access to irradiation sites at the edge of the core or even in its centre. The space available for a sample in these channels is limited to less than 2.5 cm in diameter and 15 cm length. There are also horizontal channels that lead to irradiation sites some distance from the core. They can contain different materials to modify the neutron spectrum in the particular channel. The temperature of the samples during irradiation is ranging between room temperature (25 °C) and around 50 °C. Therefore, the accumulated annealing time during irradiation (also called pre-annealing time) is not negligible. The estimation of the fluence is well established in this facility, however the infrastructure is not adapted for irradiation of full 8-inch sensors due to their size [28].

The second facility is Rhode Island Nuclear Science Center (RINSC) located in Narragansett, Rhode Island, USA. It is the only institute where the irradiation of the 8-inch wafer is possible. The facility has a 2MW, light-water cooled, pool-type reactor [30]. The irradiation of the full sensors can be done only via a beam port, which is one of the six methods of materials irradiation at RINSC. The beam port measures about 4 m from its opening to the termination near to the reactor core, and it can accommodate samples with diameters of up to 20 cm and with depths up to 90 cm. For the irradiation, sensors are placed in a special container, referred to as a "hockey puck" (fig. 4.8a). Up to four sensors can be stored in one puck. The hockey pucks with sensors are then placed in a cylinder (fig. 4.8b), which delivers the samples to the reactor core area via the beam port (fig. 4.8c). Together with the full sensors, test structures are also irradiated at RINSC. The silicon sensors are kept at low temperatures during the irradiation in order to minimise thermal annealing effect. The cooling is done with the use of dry ice, surrounding the sensors in the cylinder. In order to estimate the fluence delivered to the samples, so-called D0 diodes, pin diodes and iron foils are placed together with the main puck for each irradiation [30, 31].

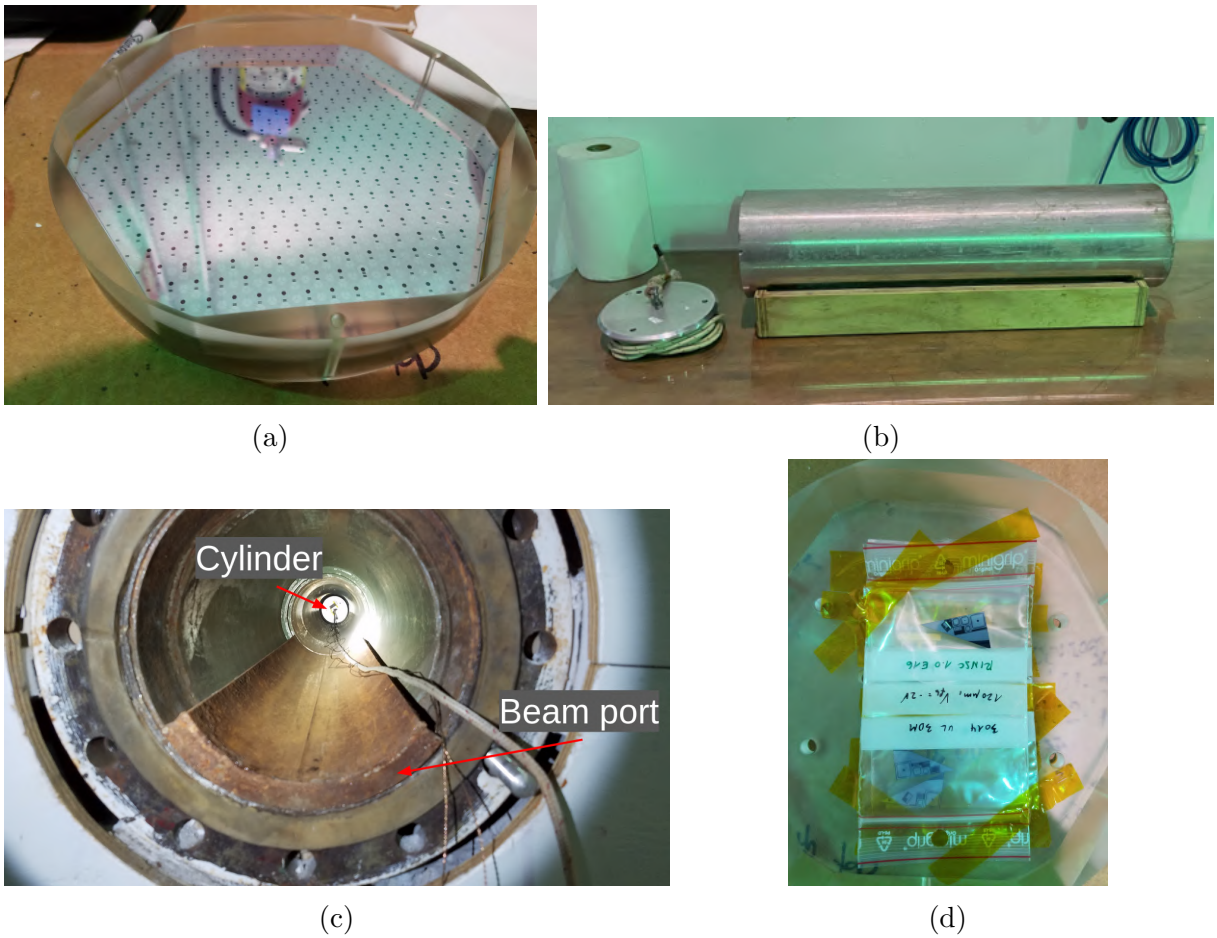

(a) (b) (c) (d)

Figure 4.8: Elements used in the RINSC irradiation facility: a) hockey puck holding sensors, b) cylinder holding the pucks, c) beam port, d) diodes attached to the puck [31].

RINSC is a new institute used for HGCAL silicon irradiation and the accuracy of the fluence estimation in this facility had to be checked. This was done as a part of the thesis project, by comparing the electrical characterisation results of the single diodes irradiated at RINSC and at JSI. The comparison is presented in the section 6.1.

4.3 Structures used in the present thesis

The thesis presents an overview of the electrical characterisation and radiation hardness qualification of the silicon sensors for the CMS Endcap Calorimeter Upgrade. During the time of the thesis work, the project was in the prototypes testing phase. There are three versions of the full sensors prototypes. Selected samples from two versions are presented in this work.

In this work selected test structures from prototype Version 1 are measured. The properties measured are: leakage current (IV), capacitance (CV) and charge collection (by TCT measurement). For the IV and CV measurements, the test structures are bare, whereas structures for the TCT measurements are mounted on printed circuit boards. The samples are irradiated at JSI in a way to cover the full fluence range expected in the CMS Endcap Calorimeter Upgrade. A list of diodes used for IV and CV measurement is shown in table 4.1.

Table 4.1: List of electrically characterised test structures presented in this work. All samples have standard oxide (-2 V flatband voltage).

Sensor ID	Thickness [µm]	Irradiation facility	Fluence [n_{eq}/cm^2]	Process
1113_UR_2D	300	RINSC	9.9e+14	FZ
1114_UR_2D	300	RINSC	1.4e+15	FZ
2114_UR_2D	200	RINSC	2.1e+15	FZ
3015_UL_3DM	120	RINSC	1.8e+15	epi
1002_UR_2D	300	JSI	6.5e+14	FZ
1002_UL_3D	300	JSI	6.5e+14	FZ
1003_UR_2D	300	JSI	1.0e+15	FZ
1003_UL_3D	300	JSI	1.0e+15	FZ
1102_UR_2D	300	JSI	1.5e+15	FZ
1102_UL_3D	300	JSI	1.5e+15	FZ
2002_UR_2D	200	JSI	1.0e+15	FZ
2002_UL_3D	200	JSI	1.0e+15	FZ
2003_UR_2D	200	JSI	1.5e+15	FZ
2003_UL_3D	200	JSI	1.5e+15	FZ
2102_UR_2D	200	JSI	2.5e+15	FZ
2102_UL_3D	200	JSI	2.5e+15	FZ
3008_UL_3D	120	JSI	1.5e+15	epi
3007_UL_3D	120	JSI	2.5e+15	epi
3003_UL_3D	120	JSI	1.0e+16	epi

The aim of this study is to check whether the fluence estimated for the test structures irradiated at RINSC are accurate. It is done by comparing them to the diodes irradiated at JSI, which reactor has a well-known neutron spectrum and fluence calibration thus can serve as reference. Electrical characterisation including an isothermal annealing study is performed here. For all diodes irradiated at RINSC, the pre-annealing time is approximate to 15±8 minutes. For the diodes irradiated at JSI, the pre-annealing time is is ranging between 5 and 110 min (depending on the fluence). Additional five annealing steps at 60 °C were performed, namely:

1. step: 25 min of additional annealing (40 min in total),
2. step: 52 min of additional annealing (92 min in total),
3. step: 23 min of additional annealing (115 min in total),
4. step: 50 min of additional annealing (165 min in total),
5. step: 215 min of additional annealing (380 min in total).

For the charge collection study, other samples from prototype Version 1 were tested. The list of diodes used is presented in table 4.2. There are three unirradiated samples used for reference. Examples of the samples measured in this campaign are shown in figure 4.9.

Table 4.2: List of test structures measured in the TCT campaign. All samples have standard oxide (-2 V flatband voltage).

Sensor ID	Thickness [µm]	Fluence [n_{eq}/cm^2]	Process
1013_UR_3D	300	0	FZ
2012_UR_3D	200	0	FZ
3001_UR_3D	120	0	epi
1002_LR_3D	300	6.5e+14	FZ
1003_LR_3D	300	1.0e+15	FZ
1102_LR_3D	300	1.5e+15	FZ
2002_LR_3D	200	1.0e+15	FZ
2003_LR_3D	200	1.5e+15	FZ
2102_LR_3D	200	2.5e+15	FZ
3008_LR_3D	120	1.5e+15	epi
3007_LR_3D	120	2.5e+15	epi
3003_LR_3D	120	1.0e+16	epi

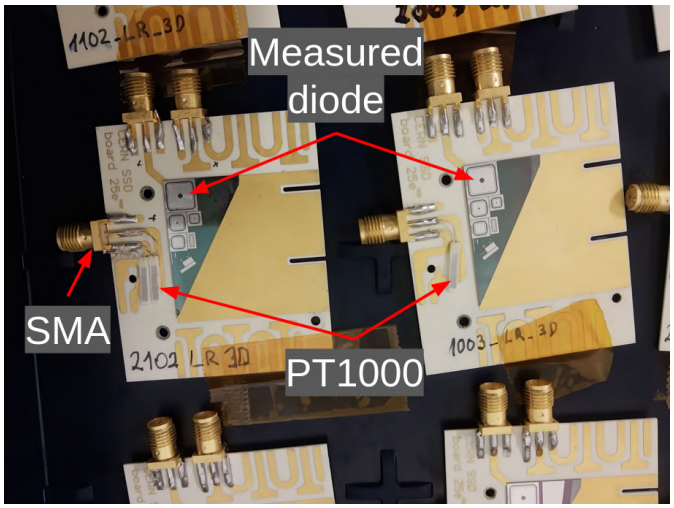

Figure 4.9: Examples of the diodes measured in the TCT campaign. The halfmoon part hosting the tested diode and few additional test structures not used in the following is mounted on a PCB for easy connection to the TCT measurement circuit.

In this measurement campaign, an efficiency of the charge collection of the samples is studied. Charge collection is extracted from recorded transient currents induced by IR-laser. The samples have the opening in the metallization for injecting laser light. The diode and the guard ring are connected with a wirebond to the SMA connector on a PCB. To control the temperature of the diode during the measurement, the PT1000 resistor is attached to the PCB close to the sample. The PT1000 is connected to the SMA connector and the resistance is converted to temperature. The property is measured at different annealing stages. All the samples used in for measuring the charge collection efficiency are irradiated at JSI and the pre-annealing times are the same as for the diodes used for IV and CV measurement. Six steps of the annealing at 60 °C were performed in this study:

1. step: 10 min of additional annealing,
2. step: 20 min of additional annealing (30 min in total),
3. step: 60 min of additional annealing (90 min in total),
4. step: 30 min of additional annealing (120 min in total),
5. step: 160 min of additional annealing (280 min in total),
6. step: 720 min of additional annealing (1000 min in total).

The full sensor electrical characterisation that is presented in this work was performed on selected samples from prototype Version 2. The difference between the two versions are not considered in this work and thus will be not described. The sensors were produced in four different oxide quality processes. The oxide types are named as follows: type A (STD, $V_{\text{fb}} = -2V$), type B (STD, $V_{\text{fb}} = -5V$), type C (thermal condition change, $V_{\text{fb}} = -2V$), type D (new combination of B and C types, $V_{\text{fb}} = -2V$). In this study, only unirradiated sensors are tested. These sensors were delivered on dicing frames. They were tested at CERN before and after removing them from dicing frames. The comparison of the results obtained in these two configurations is shown in this work. Additionally, the sensors are also tested at Hamamatsu, before sending out. These results are included in the summary as well. The electrical properties between different oxide types were also compared. A list of the full sensors measured in this study is shown in table 4.3.

Table 4.3: List of electrically characterised full sensors presented in this work.

Sensor ID	Thickness [µm]	P-Stop	Oxide type	Process
N4791_1	300	com.	A	FZ
N4791_2	300	com.	A	FZ
N4790_1	300	com.	B	FZ
N4790_2	300	com.	B	FZ
N4790_3	300	com.	B	FZ
N4791_6	300	com.	C	FZ
N4791_7	300	com.	C	FZ
N4791_8	300	com.	C	FZ
N4791_9	300	com.	C	FZ
N4791_18	300	ind.	C	FZ
N4791_19	300	ind.	C	FZ
N4791_20	300	ind.	C	FZ
N4791_21	300	ind.	C	FZ
N4790_13	300	com.	D	FZ
N4790_14	300	com.	D	FZ
N4790_15	300	com.	D	FZ

Chapter 5

Silicon sensor characterisation techniques and setups

5.1 Diode characterisation

In order to verify the quality and test the radiation damage of the HGCAL silicon sensors, they undergo a series of tests and measurements. The test structure diodes are characterised with two separate setups.

5.1.1 Current and capacitance characterisation

The first setup, the current and capacitance probe station (IV/CV), is used to determine the electrical properties of the device. The leakage current as a function of the bias voltage (also known as IV) and capacitance as a function of the bias voltage (also known as CV) are measured. Important quantities that can be obtained from these measurements are: full depletion voltage, end capacitance (capacitance beyond the full depletion) and leakage current at full depletion. In case the diode breaks through (resulting in exponentially growing current) also the so-called break down voltage can be recorded.

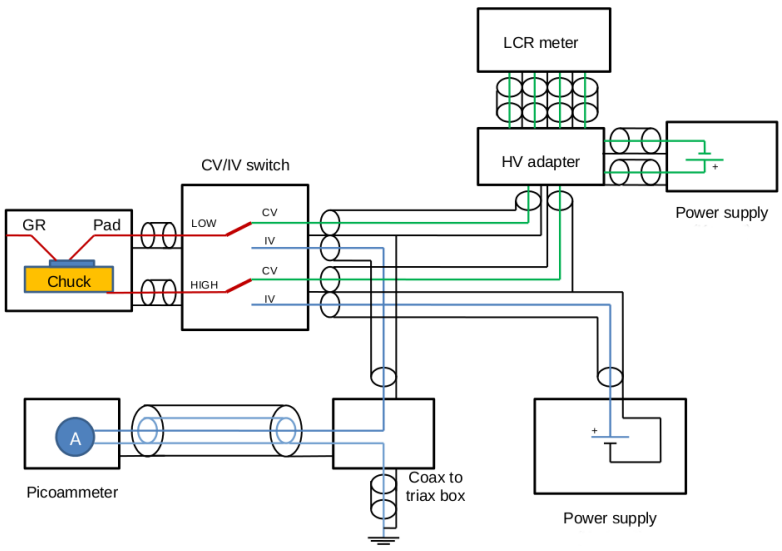

Figure 5.1: The current and capacitance characterisation setup diagram [32].

The diagram of the setup is shown in figure 5.1. For the IV part, the high voltage is provided by a power supply – Keithley 2410. Leakage current is measured by a picoammeter – Keithley 6487. In terms of CV part, the same type of device is used as a high voltage source (Keithley 2410). The readout of capacitance is done by an LCR meter (Keysight E4980A). A decoupling box (denoted as HV adapter) protects the inputs of the LCR meter from high bias voltages. The CV measurement is taken by the application of DC bias voltages across the capacitor while making the measurements with an AC signal. An AC frequency of 10 kHz is used for all measurements performed on test structure diodes. The LRC meter is measuring a phase shift and an amplitude change in the signal. To arrive at a capacitance, it is necessary to make certain assumptions regarding the circuit under measurement (parallel or series model, see [33]).

IV and CV are combined in one setup by the use of a high frequency switch (model H6P-330127), which enables automatic switching between the two measurements. According to the datasheet [34], the frequency of this device is rated up to 12.4 GHz. In terms of IV/CV setup such a high frequency is not necessary as the frequency of the CV measurements do not usually exceed 500 kHz. However, a high frequency rating is useful for the Transient Current Technique (TCT) measurements (cf. sec. 5.1.2), where fast laser pulses are used, to generate charge in the silicon sensor that are recorded time resolved with 2.5 GHz sampling.

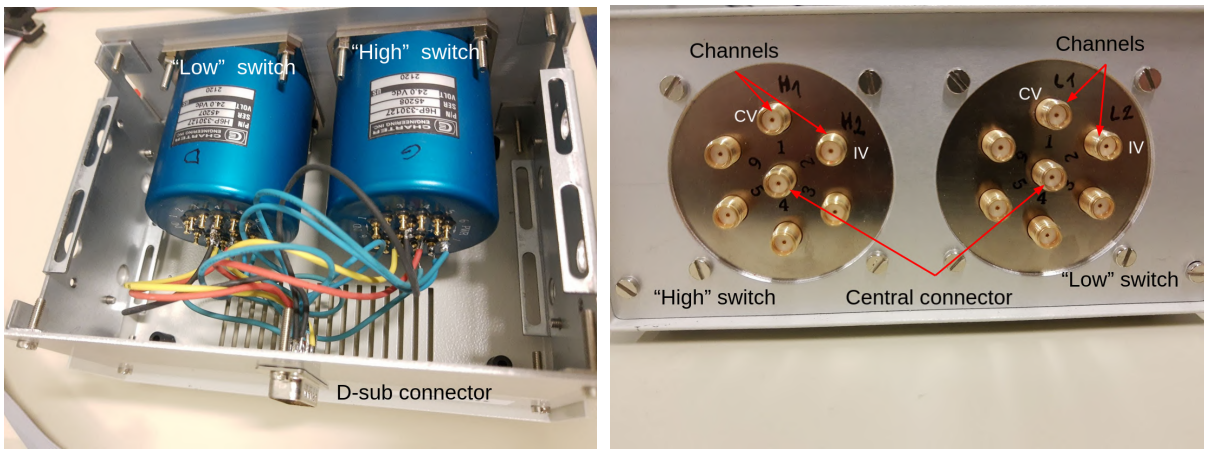

(a) (b)

Figure 5.2: Pictures of the switch box containing two high frequency switches – inside (a) and front (b) view.

The switch box shown on the setups diagram in fig. 5.1 and in figure 5.2, contains two high frequency switches which are called "high" (for high path) and "low" (for low path). The high path is used for high voltages (HV), whereas the low path is at ground potential. Each switch has a single input (central connector, cf. fig. 5.2b) that can be connected to six outputs (channels). The switch that is used in the IV/CV setup has two active outputs (channels) both for low and high paths. Channel 1 belongs to the CV measurement, while channel 2 belongs to the IV measurement. They are connected to the outputs of a multifunction input/output (i/o) device [35, 36] (USB-6000 from National Instruments), as shown in figure 5.3a. It is a data acquisition device that enables communication between the software and the switch. High and low paths for each type of measurement are connected separately to the multifunction device (cf. fig. 5.3). Switching between measurements is done by applying a voltage pulse to the respective channels. The channels

are encoded in binary code in the software as follows (cf. fig. 5.3b):

- CV measurement: 0101,
- IV measurement: 1010.

The "1" means that the respective channels (e.g. *CV High* and *CV Low* for the CV measurement) get a 3.3 V pulse for 0.5 s and are activated.

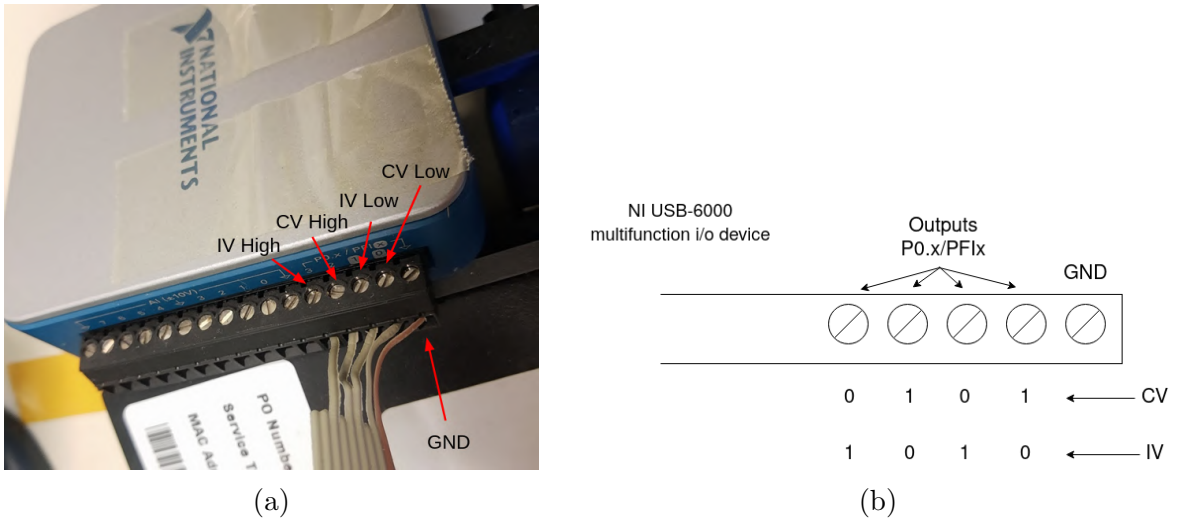

(a) (b)

Figure 5.3: (a) NI multifunction device connected to the switch channels in the IV/CV setup. (b) Schematic diagram of the connection.

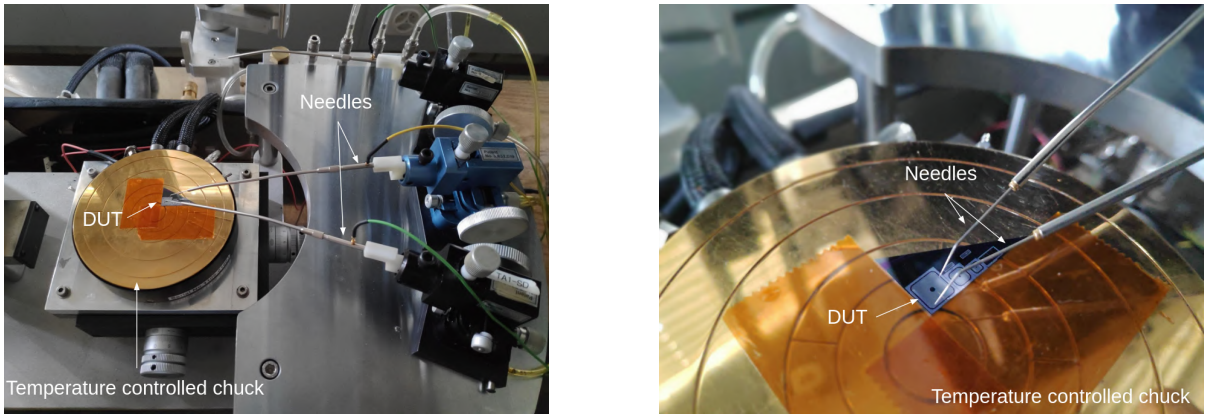

(a) (b)

Figure 5.4: Pictures of the IV/CV setup showing DUT placed on the chuck and connected by the needles.

In the IV/CV setup, a device under test (DUT), for instance a silicon diode, is placed on the chuck and connected by two needles (fig. 5.4). The chuck controls the temperature of the DUT during the measurements and enables to apply the bias voltage on the back side of the sensor. Additionally, it provides vacuum to hold the DUT in place. One of the needles is connected to the diode's pad for signal reading. The second one is connected to its guard ring. These components are located inside a Faraday cage. It protects against electromagnetic radiation and minimises the amount of light coming to the DUT. Additionally, dry air flushing the Faraday cage prevents condensation at cold temperatures [37].

5.1.2 Transient Current Technique

Transient Current Technique setup (TCT+) is the second setup for characterisation of the test structures. It uses laser pulses to induce charge carriers in the silicon. The generated carriers drift towards the respective electrodes, where the bias voltage is applied. Time resolved induced currents are recorded as function of the bias voltage and analysed. This current is measured as voltage signal by an oscilloscope at an input resistance of 50 Ω. The measurement provides information on many detector properties such as: signal formation, drift velocity, electric field configuration, carriers trapping times and charge collection efficiency. Time resolved induced current can be determined by applying Ramo's theorem, cf. equation 5.1 [38].

$$I(t) = -q \cdot \vec{v} \cdot \vec{E_W} \tag{5.1}$$

In equation 5.1, $\vec{v} = \vec{v}(\vec{E})$ is the drift velocity, $\vec{E}$ is the electric field and $\vec{E_W}$ is the so-called weighting field. The electric field defines the charge trajectory and the velocity of the particle. A schematic view of the TCT+ setup is shown in figure 5.5. The setup gives the possibility to choose between two laser wavelengths: 660 nm (red) and 1064 nm (infra-red). Light can be injected from the front or back side of a DUT. For the infra-red laser, light can in addition be injected from the edge. However, all measurements presented in this work are performed using the infra-red front laser, therefore a simplified diagram of the setup with only one, used, configuration is shown.

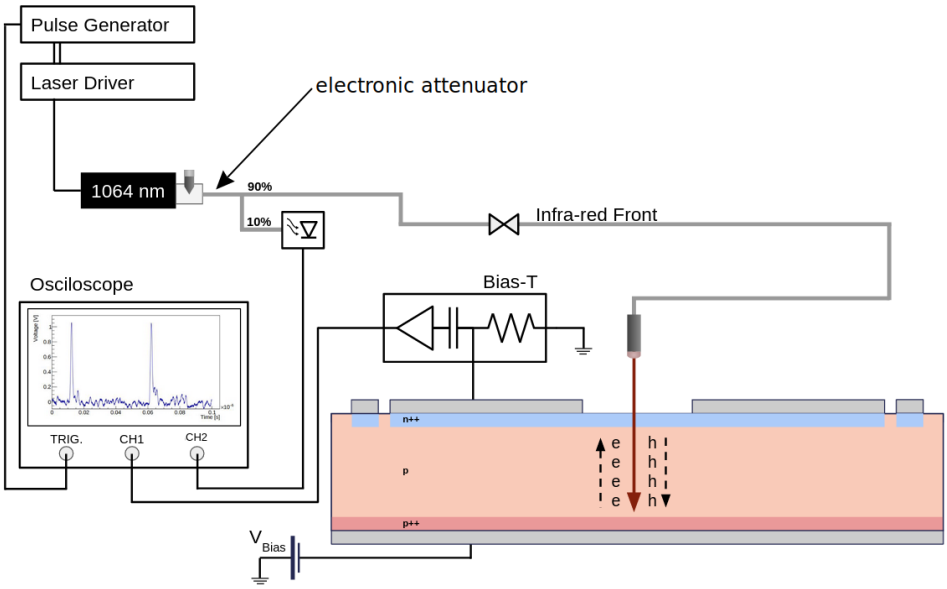

Figure 5.5: TCT+ setup diagram [39].

In the TCT+ setup, the DUT has to be attached to a PCB and wire-bonded. The PCB contains also a reference PT1000 resistor, which inform the software and the user about the temperature near the sensor area. For the measurement, the PCB is mounted on a copper holder and connected by coaxial cables (fig. 5.6). The holder is cooled by a Peltier element connected to a chiller. Part of the setup is placed inside a Faraday cage (fig. 5.7), equipped with a dry air flush, which has the same role as in the IV/CV setup. An XYZ stage system enables adjusting the laser focus (Z coordinate, vertical) and the position (X,Y coordinates) of the DUT. The laser light is coming from the laser head to the DUT through optical fibers and a lens. Its intensity can be modulated by

an electronic attenuator. The light is split into two lines, 10% is sent to a reference photodiode for measuring its intensity while the remaining 90% is used for the DUT illumination. The sensor is biased from the back side using a Keithley 2410 power source. The generated current as well as the signal from the reference photodiode are readout by an Agilent DSO9254A oscilloscope. The DUT signal is amplified by a CIVIDEC C2-HV amplifier [40], which contains an integrated Bias-Tee. It allows to read the signal while protecting the oscilloscope from the high voltage [37]. In this work, the TCT+ setup is used for studies on charge collection only.

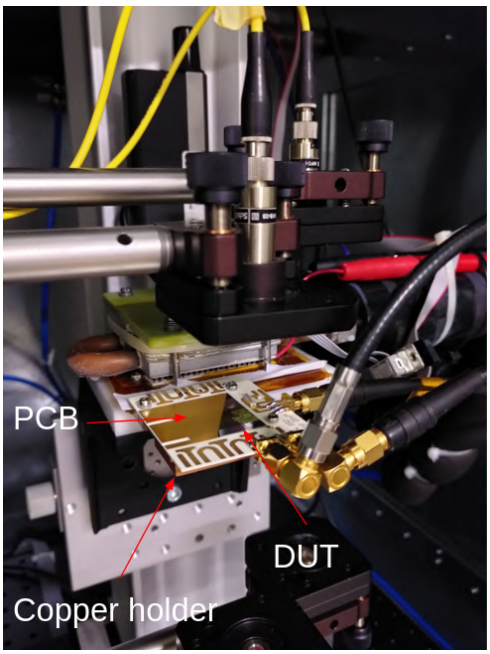

Figure 5.6: A DUT placed on a PCB and mounted on a copper holder inside the Faraday cage.

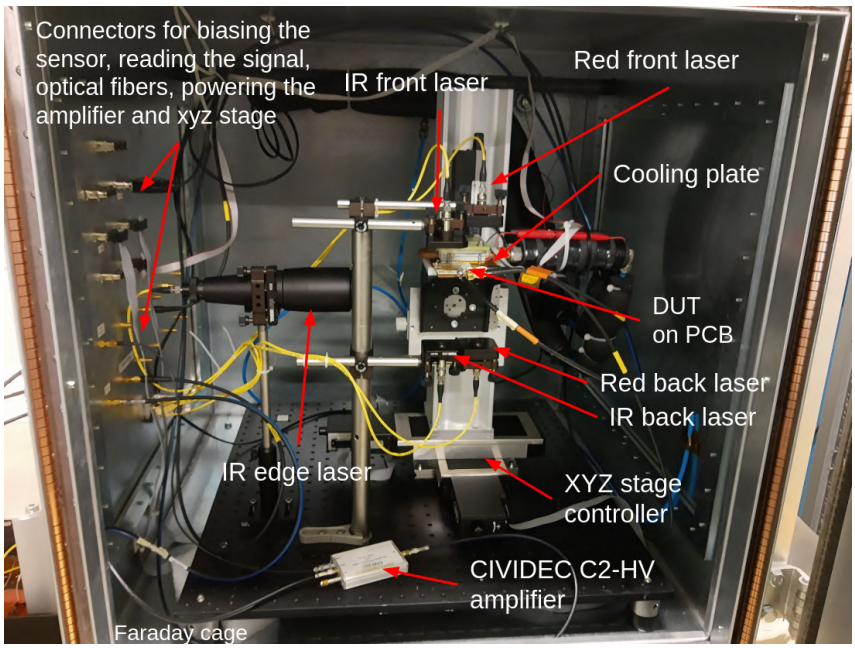

Figure 5.7: Components of the TCT setup inside the Faraday cage.

5.2 Full-sensor characterisation

Along with the test structures, the full wafers are also electrically characterised. In the IV and CV measurement, cells should be tested individually and the bias voltage has to be applied to all pads simultaneously (similarly to the operating conditions at the experiment). This allows for a coherent electric field configuration inside the sensor. To fulfill this requirement, a switch- and probe-card-based system for silicon sensor characterisation was developed at CERN. The system is called ARRAY (switching mAtRix pRobe cArd sYstem) [41].

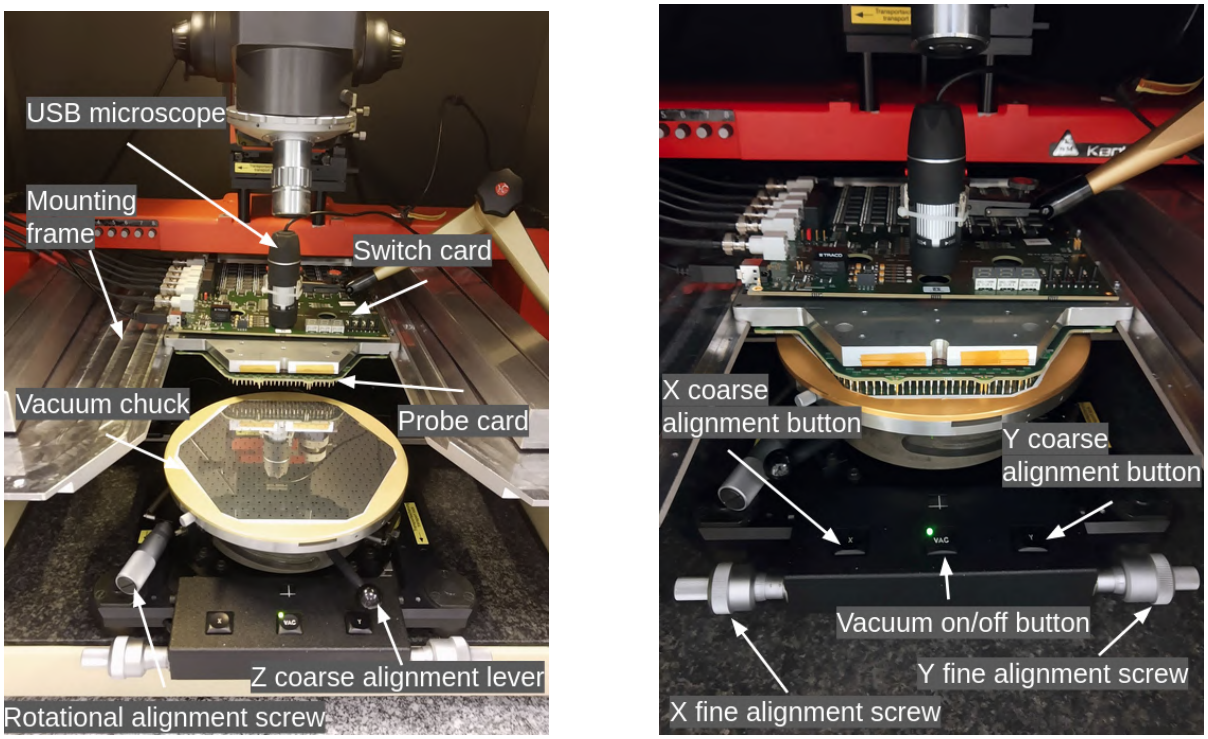

(a) (b)

Figure 5.8: Probe station for full wafer characterisation with the ARRAY system, before (a) and after (b) the alignment and contacting procedure.

The switch card is an active matrix with 512 input channels designed as a plug-in PCB, which is installed on the top of the probe card [41]. The switch card is an array of multiplexers that controls the measurement. The probe card is a passive element, which has spring-loaded pogo pins mounted on its surface. They enable the connectivity to the sensor for all individual sensor cells. The two cards are mechanically attached to a probe station, as shown in figure 5.8. The sensor is placed on a chuck and hold in place by a vacuum. The setup contains several tools for aligning and contacting the DUT to the pins of the probe card. These are an USB microscope (as a visual support), XY coarse alignment buttons, Z coarse alignment lever as well as XYZ and rotational (theta) fine alignment screws. The probe station is located inside a dark box, which minimises the amount of light during the measurement and thus prevents inducing dark currents in the silicon. The dark box also acts as Faraday cage [14, 41].

A computer visualisation of the two main elements of the ARRAY system – probe card with switch card plugged in on top, is shown in figure 5.9a. The probe card has an array of spring-loaded pins with 1.4 mm travel range that are used to contact all individual sensor

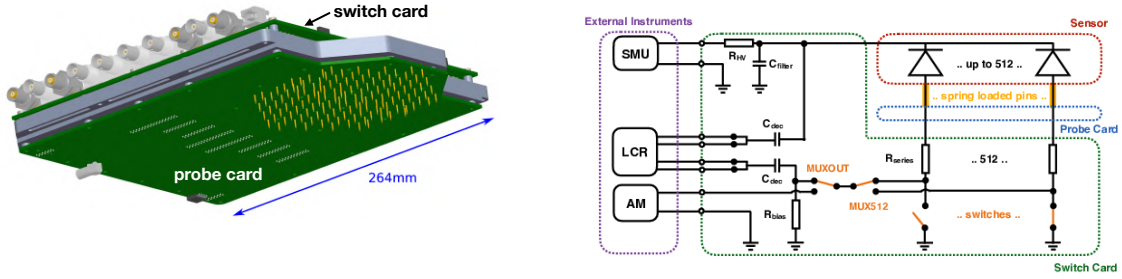

(a) (b)

Figure 5.9: (a) CAD drawing of the probe card with the plug-in switch card on the top [17]. (b) A simplified circuit diagram of the ARRAY system [41].

pads. The travel range prevents damaging the pads during contact and ensures a uniform contact across the full sensor area. The pins have a rounded tip with a radius of 250 µm. In order to provide a proper electrical contact to the aluminium pads on the sensor, a force of around 25 g per pin has to be applied [41]. It is done via the mechanical integration into the probe station. The probe card contains also several test capacitances for system calibration and crosschecks as well as humidity and temperature sensors for monitoring environmental conditions. The card is mechanically installed into a steel mounting frame (fig. 5.8). A simplified circuit diagram of the full system is shown in figure 5.9b. 10 kΩ resistors (R_{series}) are inserted in series to the pins inside the switch card to protect against high currents that may occur in the measurement. The signal coming from the pins is routed via multiplexer with 512 channels (MUX512) towards the readout instruments [41]. The output multiplexer (MUXOUT) allows automatic switching between the leakage current and capacitance measurement circuits. The switch card contains six coaxial BNC connections for external instruments – the power supply (Keithley 2410, indicated as SMU in the figure 5.9b), LCR meter (Keysight E4980A, indicated as LCR) and the picoammeter (Keithley 6487, indicated as AM). Two 1 µF capacitors (C_{dec}) have the same function as the decoupling box in the IV/CV probe station (sec. 5.1.1) – they are used to decouple the LCR meter from the high DC bias voltage. Communication with the switch card is possible through a built-in microprocessor and USB interface [14, 41].

Chapter 6

Results of HGCAL test structure diodes and full sensors

6.1 Electrical characterisation of test structure diodes

Electrical characterisation of the test structure diodes consist of leakage current (IV) and capacitance (CV) measurements. Both properties are measured as a function of the bias voltage ranged between -20 V and -900 V. As discussed in section 4.3, the electrical properties of the samples irradiated at JSI and RINSC are measured and compared, including an isothermal annealing study. An example of the IV and CV results for 200 µm diodes at 120 min of total annealing time at 60 °C is presented in figure 6.1. All measurement presented in this section are performed at -20 °C.

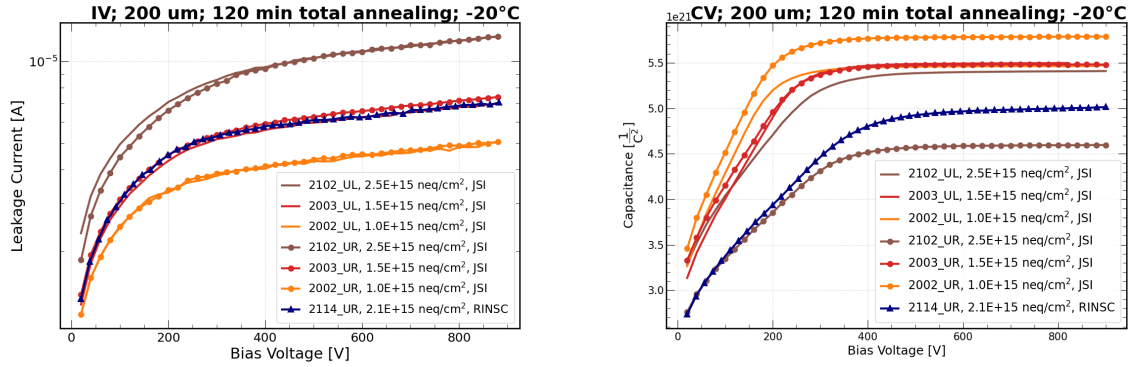

(a) (b)

Figure 6.1: a) IV and b) CV exemplary results for 200 µm thick sensors at 120 min of total annealing time [42].

The leakage current is in order of few µA for 200 µm sensors. The difference of the leakage current value between the samples comes from the fact that they are irradiated to different fluences. The higher the fluence, the higher the leakage current. The samples irradiated at JSI are assumed to be reference samples i.e. their fluences are determined with very good precision. The one diode in this plot that was irradiated at RINSC (2114 UR) has almost the same leakage current than the samples 2003 UR and UL. However, according to the information about the fluences reported by RINSC, the fluence between these samples are not the same or similar. This result indicates that the fluences

were not correctly determined at RINSC. The capacitance results are presented as inverse capacitance squared ($1/C^2$) as a function of the bias voltage. From this plot the depletion voltage value can be obtained by the intersection of the two lines – fit of the raising linear part (before depletion) and fit of the constant part (after depletion, when the plateau is reached). The depletion voltage increases as the fluence increases.

The leakage current values at the bias voltage equal to depletion voltage as a function of the annealing time at 60 °C are shown in figure 6.2. Each plot presents sensors of one thickness. The figure 6.2a present results for 300 µm sensors – 6 irradiated at JSI

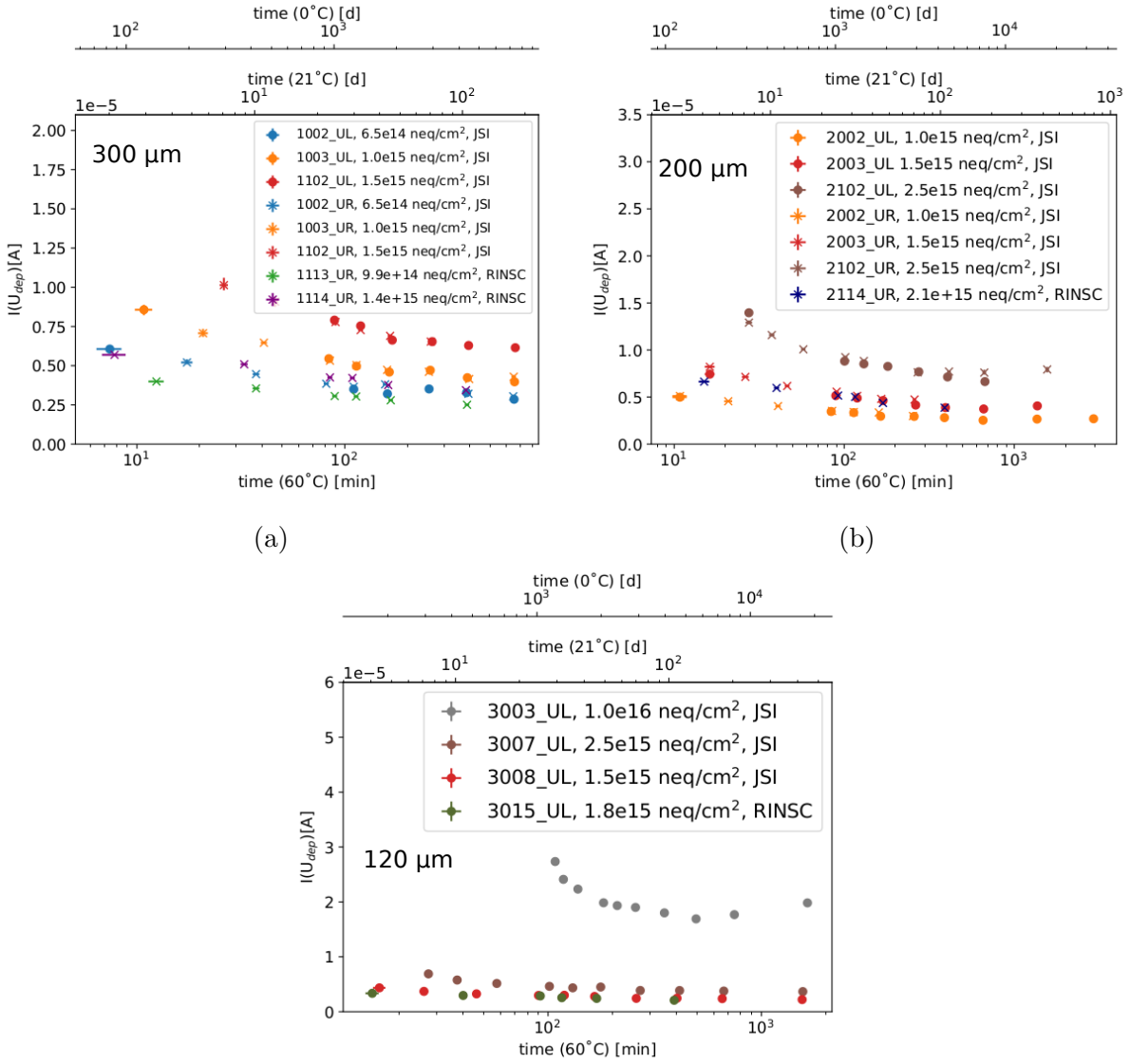

Figure 6.2: Leakage current at depletion voltage as a function of annealing time at 60 °C for a) 300 µm, b) 200 µm and c) 120 µm sensors [43].

and 2 irradiated at RINSC. The samples are irradiated to 3 fluences at JSI (6.5e+14, 1.0e+15 and 1.5e+15 n_{eq}/cm^2) and determine the leakage current levels at these fluences. Looking at the samples from RINSC, a discrepancy between fluence information can be observed. The sample 1113 UR (green color in the plot), which fluence is given as 9.9e+14 n_{eq}/cm^2, should be close to samples 1003 UR and UL (marked as orange), as

their fluence is equal to 1.0e+15 n_{eq}/cm^2. However, it is not the case. The leakage current of the sample from RINSC is around 45% lower than the reference sample from JSI, it is even below the samples irradiated at JSI to 6.5e+14 n_{eq}/cm^2. Similar observations can be made by analyzing the second sample from RINSC – 1114 UR (purple color), irradiated to 1.4e+15 n_{eq}/cm^2, which should be close to the samples 1102 UR and UL (marked as red) irradiated to 1.5e+15. The leakage current in this case is around 34% lower than the respective reference sample. For the 200 µm sensors (shown in fig. 6.2b) the discrepancy also can be seen. The sample 2114 UR from RINSC, which is reported to be irradiated to 2.1e+15 n_{eq}/cm^2 has similar leakage current level as the samples 2003 UR and UL, irradiated at JSI to 1.5e+15 n_{eq}/cm^2. It is the case for 120 µm sensors (fig. 6.2c) as well. The sample 3015 UL, irradiated to 1.8e+15 n_{eq}/cm^2 at RINSC, is on the same level of the leakage current or even a bit lower as the sample 3008 UL, which is irradiated at JSI to 1.5e+15 n_{eq}/cm^2.

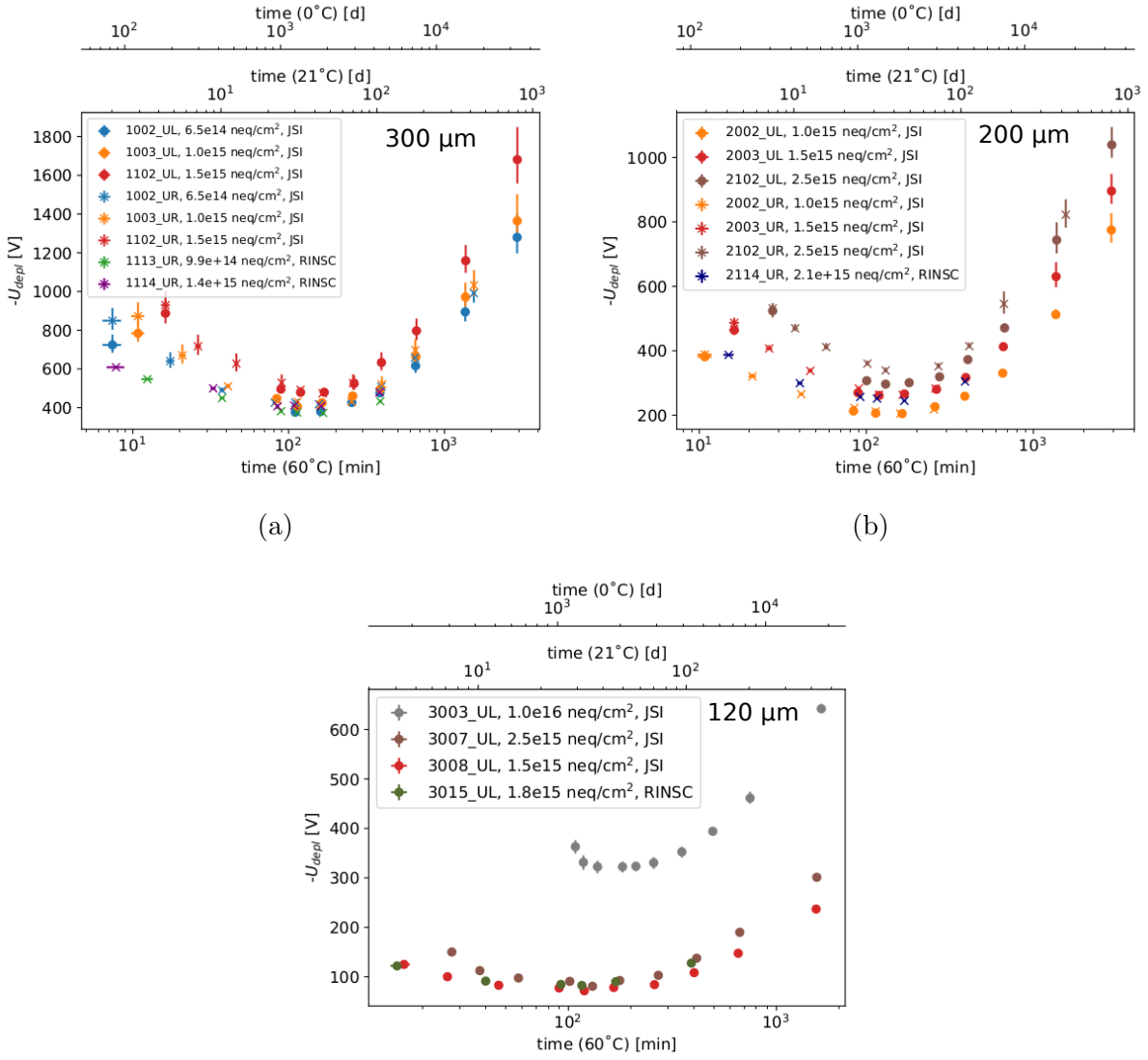

Figure 6.3: Depletion voltage as a function of annealing time at 60 °C for a) 300 µm, b) 200 µm and c) 120 µm sensors [43].

The figure 6.3 presents depletion voltage values as a function of the annealing time at 60 °C, each plot for particular sensor's thickness. The first part of the plot shows an effect of beneficial annealing, when the depletion voltage is decreasing. The minimum is reached at around 100 min at 60 °C for all thicknesses. Annealing above this value results in increasing the depletion voltage, which is an effect of reverse annealing. Annealing time at 60 °C can be converted to equivalent annealing time at a different, target temperature, for example room temperature or 0 °C. It can help to predict for how much time the sensor can be annealed during its lifetime at HL-LHC to avoid reverse annealing. At lower temperatures the annealing effects are slower.

By performing the electrical characterisation of the sensors it is possible to calculate the current related radiation damage (α, cf. sec. 3.3). The alpha value was determined for all annealing steps, separately for samples irradiated at JSI and RINSC. The figure 6.4a shows an example of fitting the alpha value for one annealing stage of sensors irradiated at RINSC. The relation between alpha value and annealing time for all samples is shown in figure 6.4b. It is clearly seen that the alpha values for the samples irradiated at RINSC are lower by a fraction of 2/3 than corresponding values for the diodes irradiated at JSI.

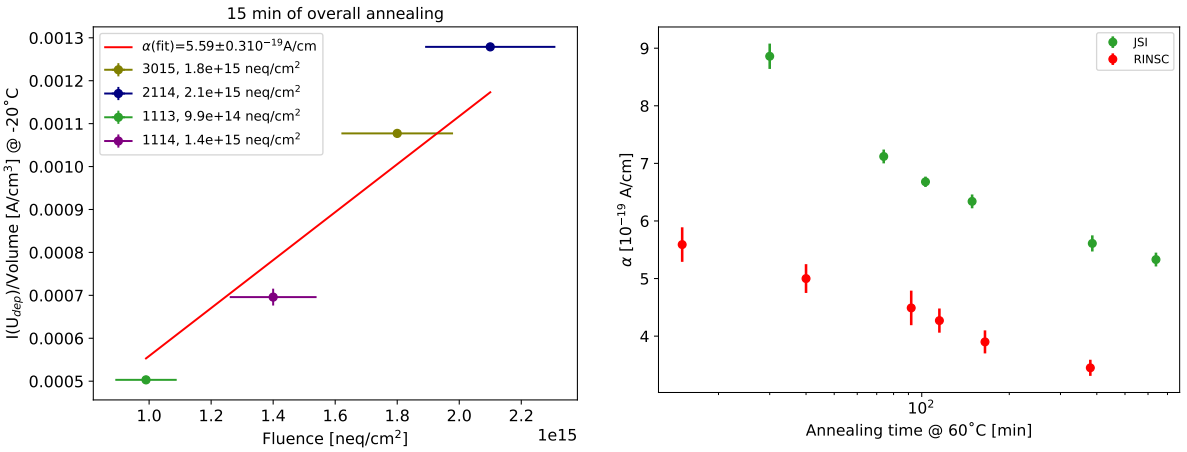

(a) (b)

Figure 6.4: a) Estimation of alpha value for samples irradiated at RINSC at no additional annealing (only pre-annealing time). b) Comparison of alpha values for samples irradiated at JSI and RINSC for all annealing steps performed [43].

The presented comparison of electrical properties between samples irradiated at JSI and RINSC explicitly show a discrepancy of fluence estimation at the two institutes. As the JSI is well established irradiation site, it is assumed that the precision of determining the fluence at RINSC is not satisfactory. The real fluence appears to be lower than it is reported. The RINSC fluence estimation could be corrected.

6.2 Charge collection of test structure diodes

Next to electrical characterisation of the test structures, a charge collection study is performed with the use of the TCT setup (cf. sec 5.1.2). In order to obtain the collected charge of the irradiated diodes, laser induced transient currents were recorded. All measurements presented in this section were performed at -20 °C, both for irradiated and unirradiated (reference) samples. Transient currents of the samples were measured for

reverse bias voltages from 0 V to 1000 V with 10 V step. The laser spot was focused at the metallization opening located in the center of the diode (cf. fig. 4.9). Example waveforms for selected bias voltages of one 300 µm sensor after 10 min of annealing at 60 °C is shown in figure 6.5a. Each waveform is measured 1000 times and averaged.

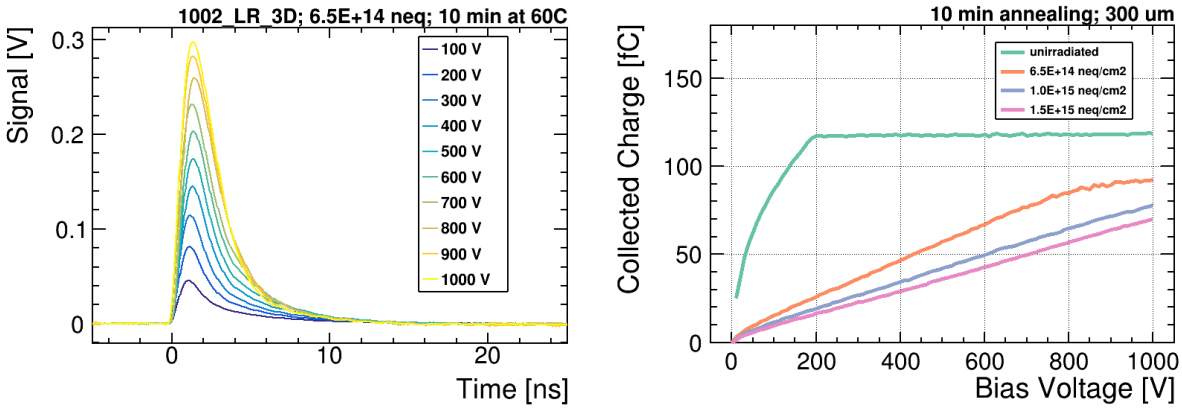

(a) (b)

Figure 6.5: Results of TCT measurements: a) Exemplary TCT signal shapes for selected bias voltages for sensor 1002 LR at 10 min of the annealing at 60 °C. b) Charge collection as a function of the bias voltage for 300 µm samples at 10 min of the annealing at 60 °C [44].

The collected charge is calculated by integrating the TCT signal over time (between 0 and 25 ns) for each bias voltage. Then, the charge collection as a function of the bias voltage can be plotted as shown in figure 6.5b. The figure presents the collected charge for 300 µm diodes (1 reference and 3 irradiated samples) at 10 min of the annealing at 60 °C. From the collected charge for all thicknesses and annealing steps, the charge collection efficiency is extracted. It is defined as the ratio of collected charge of an irradiated sample and the collected charge of the reference (unirradiated) sample of the same thickness. The charge collection efficiency at 90 min of annealing as a function of the fluence at the bias voltage of 600 V for all nine measured samples is shown in figure 6.6a.

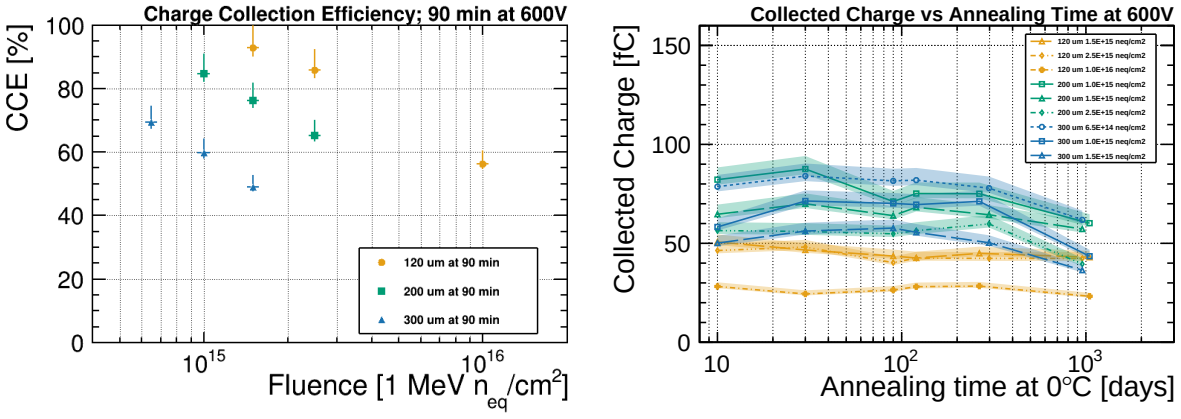

(a) (b)

Figure 6.6: Results of TCT measurements: a) Charge collection efficiency as a function of the fluence at 90 min of the annealing. b) Charge collection as a function of the annealing time [44].

The efficiency is decreasing with the fluence. The 300 µm diodes were irradiated to the lowest doses and they have the charge collection efficiency ranging between around 70% and 50%. For the 200 µm diodes, it is between 85% and 65%. The 120 µm samples, which were irradiated up to 1.0e+16 n_{eq}/cm^2, exhibit the charge collection efficiency ranging between around 90% and 60%. One sample for each thickness was irradiated to 1.5e+15 n_{eq}/cm^2. By analyzing this fluence point, it can be observed that the thinner the diode, the higher the charge collection efficiency. Therefore, the 120 µm will be located in the highest radiation regions in the HGCAL.

In addition, the collected charge of all irradiated samples is plotted as a function of the annealing time at the bias voltage of 600 V, as shown in figure 6.6b. The color bands represent the error bars. In this plot, the annealing time is scaled to days at 0 °C. The collected charge for 300 µm and 200 µm diodes ranges between around 50 fC to 90 fC, whereas for 120 µm – between 30 fC and 50 fC. This plot shows that charge collection does not change significantly with annealing time.

6.3 Electrical characterisation of full sensors

Electrical characterisation of the full sensor, as for the diodes, include leakage current and capacitance measurements. Leakage current is measured as a function of the bias voltage ranged between -25 V and -850 V. After the measurement the results are processed and analysed. This procedure includes grading of the sensor, which determines whether the sensor fulfills specified requirements. For the non-irradiated sensors, there are four global criteria:

- the total current at 600 V (normalised to 20 °C) is less than or equal to 100 µA,
- the total current at 800 V is less than 2.5 times the total current at 600 V,
- the number of bad pads is less than or equal to 8 for full-sized sensors,
- the allowed number of adjacent bad pads is less than or equal to 2.

Total current is measured as the average of the total current of the last 50 channels. To define bad pads, a per-pad characteristics is used. A pad is designated as bad if any of the following criteria is met:

- the pad current at 600 V (normalised to 20 °C) is greater than 100 nA,
- the pad current at 600 V is greater than 10 nA and pad current at 800 V is greater than 2.5 times the current at 600 V,
- the pad current at 600 V is less than or equal to 10 nA and pad current at 800 V is greater than 25 nA.

An example of IV grading result for one sensor is shown in figure 6.7.

Results of the IV measurement can be presented in several ways. One of them is so-called “hexplot”, which is a channel map with pad currents depicted as a colour scale with numerical values shown. If a pad’s current is above the scale, then it is marked as red. A hexplot is done for particular bias voltage. An example of two hexplots showing leakage current measured at bias voltage of 600 V is presented in figure 6.8. On this type of plot, one can easy find outliers with high leakage current and observe if the current

Grading:

- Sensor has been graded with checksCollectionID 6.
- Global characteristics:
  - Current at 600V I600 (normalised to 20 deg Celsius): <= 100 μA integrated over the sensor and guard rings: Passed
  - I800 < 2.5 x I600: Passed
  - Number of bad pads 0 <= 8 for full-sized sensors: Passed
  - Allowed number of adjacent bad pads <= 2: Passed
- Per-pad characteristics used to define bad pads if any of the following are met:
  - Current at 600V I600 (normalised to 20 deg Celsius) > 100 nA/pad: **0** pads, namely **[]**
  - I600 > 10 nA and I800 > 2.5 x I600: **0** pads, namely **[]**
  - I600 $\leq$ 10 nA and I800 > 25 nA: **0** pads, namely **[]**

Sensor has PASSED the requirements.
WARNING: The following pads were masked at least once before or at 600V: [].

Figure 6.7: IV grading example for sensor N4791_6 measured at CERN on dicing frame [26].

is homogeneous across the sensor. For the unirradiated sensors, the leakage current is in order of few nA, what can be seen in the presented hexplot. According to the grading requirements for pads, leakage current at 600 V should be lower than 100 nA.

Another way of presenting IV results is a plot showing measured leakage current as a function of the bias voltage for all cells. Exemplary two plots are shown in figure 6.9. The 100 nA limit is marked as a red dashed line. One can observe how the leakage current value is growing with raising bias voltage. It is clearly visible that a group of cells has about one order of magnitude lower leakage current than most of the cells. Looking at the hexplot, these pads are the inner calibration cells of smaller surface area. Additionally, one cell (the guard ring) has significantly higher current, but still below the limit. On the same type of plot the total current is presented, as in figure 6.10. The 100 µA limit is also marked as a red dashed line. The two global criteria for the sensor's grading can be checked with the help of this plot. In the presented example, the total current is well below the limit and the increase in the total current between 600 V and 800 V points is lower than 150%. Presented examples are from two sensors that exhibit excellent IV results. The total leakage current is well below the limit and there are no outliers. The sensors pass the grading. Such results are desirable for all tested prototypes.

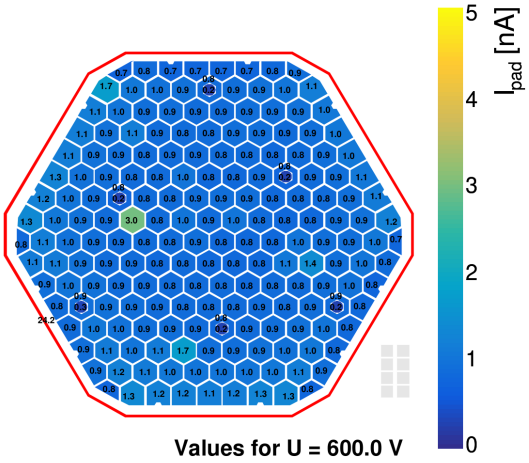

(a) Sensor ID: N4791_6

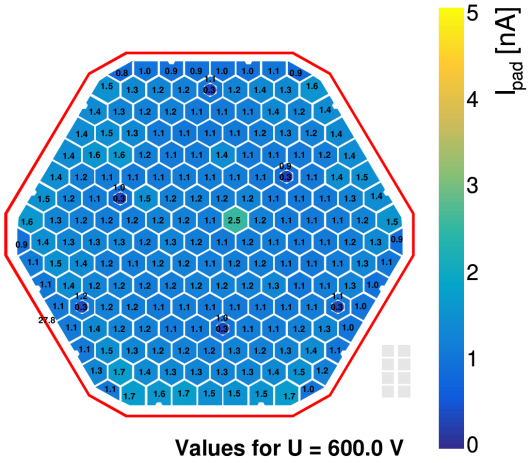

(b) Sensor ID: N4790_3

Figure 6.8: Exemplary hexplots showing measured leakage current at bias voltage of 600 V for two sensors [26].

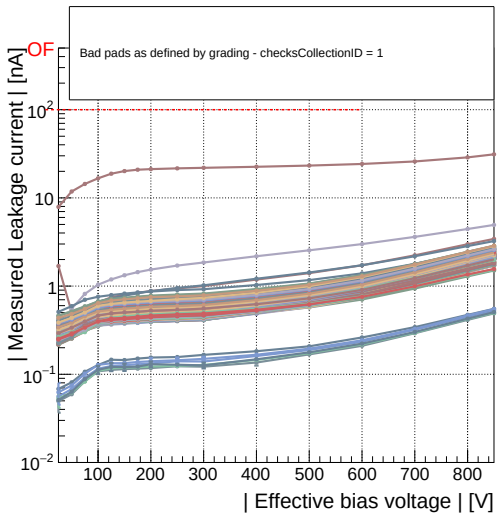

(a) Sensor ID: N4791_6

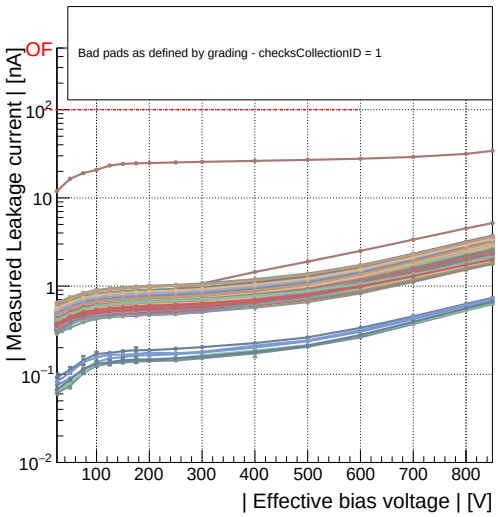

(b) Sensor ID: N4790_3

Figure 6.9: Exemplary plots showing IV curves for all channels of two sensors [26].

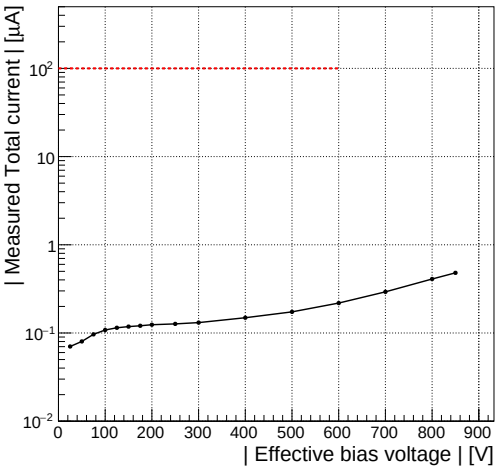

(a) Sensor ID: N4791_6

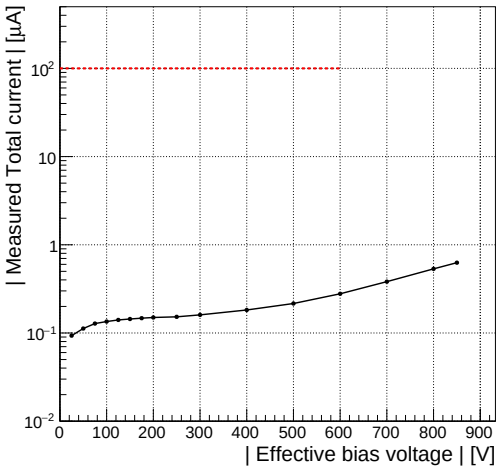

(b) Sensor ID: N4790_3

Figure 6.10: Exemplary plots showing total current curve for two sensors [26].

Each sensor from the table 4.3 was measured and analysed as described above. As mentioned in the section 4.3, the sensors were measured at room temperature in three configurations – at Hamamatsu and at CERN before and after dicing frame removal (on and off dicing frame), except for four oxide C individual p-stop sensors, which were not measured at CERN on dicing frame. All those measurements can be summarized in plots presented in figures 6.11 and 6.12. They are showing the distribution of the pad current at 600 V in the form of a boxplot, guard ring current and total current as a function of the bias voltage for all tested sensors in all three configurations. The tables 6.1, 6.2 and 6.3 are showing grading results for the sensors measured at Hamamatsu, at CERN on dicing frame and at CERN off dicing frame, respectively. In the tables, sensors of different oxide types are visually separated.

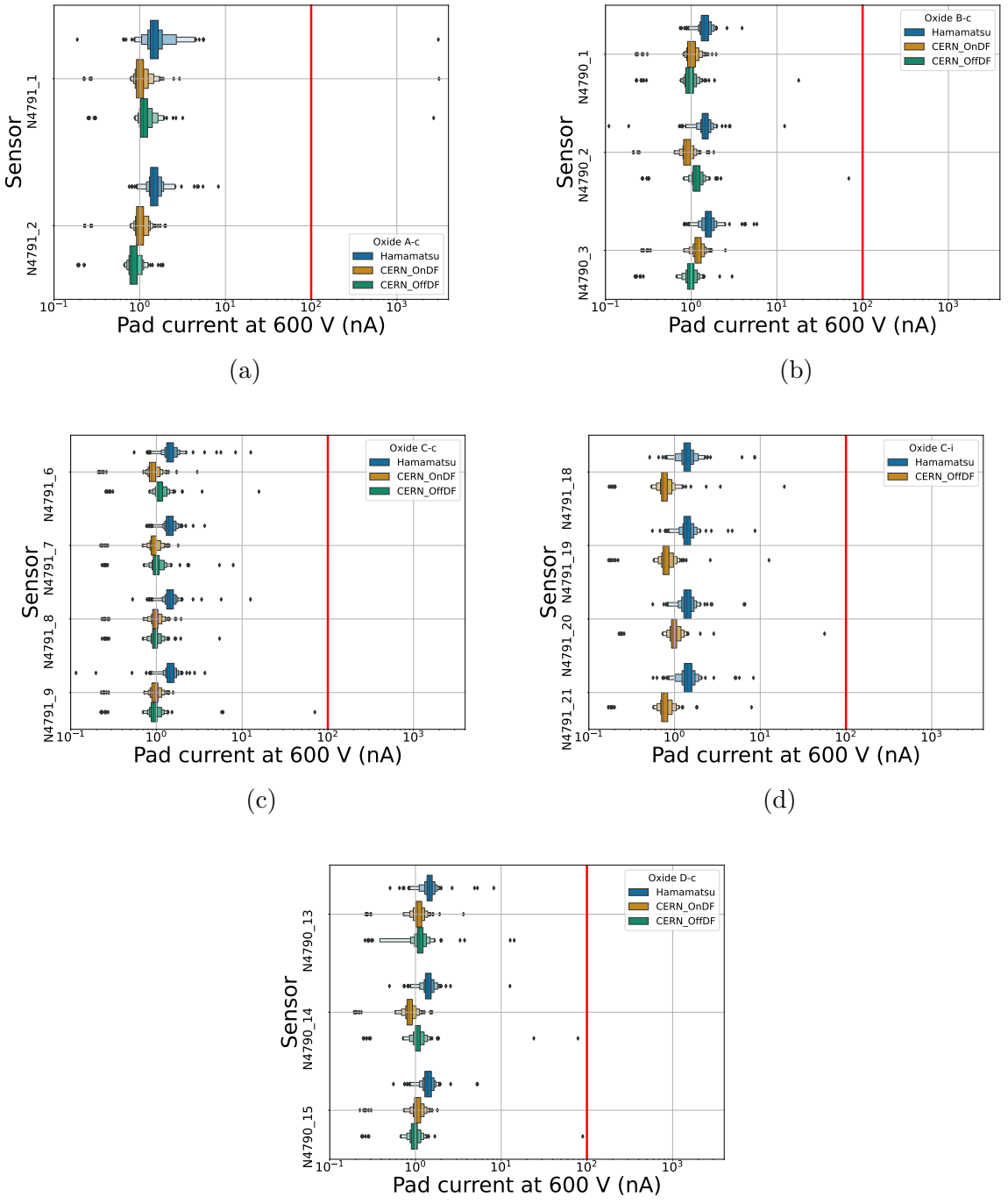

Figure 6.11: Summary of pad current at 600 V for HPK, on DF, off DF. The lowercase letters added to oxide types indicate p-stop type: c – common, i – individual p-stop.

The median value of the pad current is around 1 nA for all measurements. For Hamamatsu measurements it is slightly higher, what can be caused by a slight temperature difference of the measurements. The number of outliers is in general the same for all configurations. There is small number of cells that are above the 100 nA limit. In terms of the pad current, the results agree between all configurations. The guard ring current at CERN on dicing frame tends to be higher than at Hamamatsu as the HPK measurements

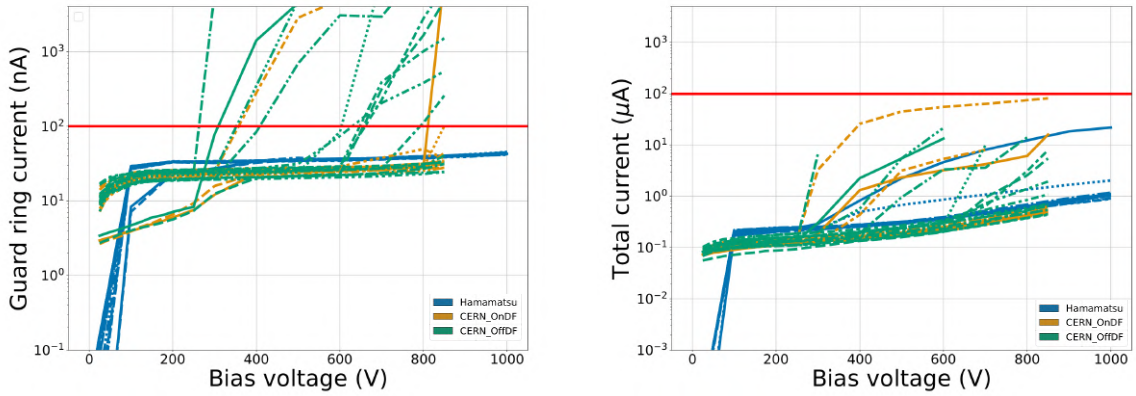

(a) (b)

Figure 6.12: Summary of guard ring current and total current for HPK, on DF, off DF.

Table 6.1: IV grading results of the sensors measured at Hamamatsu.

Sensor ID	I_{tot} at 600V < 100 µA	I_{tot} at 800V $< 2.5 \cdot I_{tot}$ at 600V	N_{cell} with $I_{600V} < 100$nA	N_{cell} with $I_{800V} < 2.5 \cdot I_{600V}$ and $I_{600V} < 10$nA	More than 8 bad cells	More than 2 adjacent cells bad
N4791_1	Passed	**Failed**	1	0	Passed	Passed
N4791_2	Passed	Passed	0	0	Passed	Passed
N4790_1	Passed	Passed	0	0	Passed	Passed
N4790_2	Passed	Passed	0	0	Passed	Passed
N4790_3	Passed	Passed	0	0	Passed	Passed
N4791_6	Passed	Passed	0	0	Passed	Passed
N4791_7	Passed	Passed	0	0	Passed	Passed
N4791_8	Passed	Passed	0	0	Passed	Passed
N4791_9	Passed	Passed	0	0	Passed	Passed
N4791_18	Passed	Passed	0	0	Passed	Passed
N4791_19	Passed	Passed	0	0	Passed	Passed
N4791_20	Passed	Passed	0	0	Passed	Passed
N4791_21	Passed	Passed	0	0	Passed	Passed
N4790_13	Passed	Passed	0	0	Passed	Passed
N4790_14	Passed	Passed	0	0	Passed	Passed
N4790_15	Passed	Passed	0	0	Passed	Passed

were done before dicing. Removing the sensors from dicing frames worsened the guard ring current significantly. Many of these sensors have the guard ring current well above the 100 nA limit, even at low voltages. The total current at CERN on and (especially) off dicing frame is also higher than at Hamamatsu, what is driven by the guard ring current.

Regarding the grading results for Hamamatsu measurements, 1 out of 16 sensors failed. The total current of the sensor N4791_1 (oxide type 'A') increases by more than 150% between 600 V and 800 V. The results at CERN on dicing frame agree with previous

Table 6.2: IV grading results of the sensors measured at CERN on dicing frame.

Sensor ID	I_{tot} at 600V < 100 µA	I_{tot} at 800V $< 2.5 \cdot I_{tot}$ at 600V	N_{cell} with $I_{600V} < 100$nA	N_{cell} with $I_{800V} < 2.5 \cdot I_{600V}$ and $I_{600V} < 10$nA	More than 8 bad cells	More than 2 adjacent cells bad
N4791_1	Passed	**Failed**	1	1	Passed	Passed
N4791_2	Passed	Passed	0	0	Passed	Passed
N4790_1	Passed	Passed	0	0	Passed	Passed
N4790_2	Passed	Passed	1	0	Passed	Passed
N4790_3	Passed	Passed	0	0	Passed	Passed
N4791_6	Passed	Passed	0	0	Passed	Passed
N4791_7	Passed	Passed	0	0	Passed	Passed
N4791_8	Passed	Passed	0	0	Passed	Passed
N4791_9	Passed	Passed	0	0	Passed	Passed
N4790_13	Passed	Passed	1	0	Passed	Passed
N4790_14	Passed	Passed	0	0	Passed	Passed
N4790_15	Passed	Passed	0	0	Passed	Passed

Table 6.3: IV grading results of the sensors measured at CERN off dicing frame.

Sensor ID	I_{tot} at 600V < 100 µA	I_{tot} at 800V $< 2.5 \cdot I_{tot}$ at 600V	N_{cell} with $I_{600V} < 100$nA	N_{cell} with $I_{800V} < 2.5 \cdot I_{600V}$ and $I_{600V} < 10$nA	More than 8 bad cells	More than 2 adjacent cells bad
N4791_1	Passed	Passed	2	0	Passed	Passed
N4791_2	Passed	**Failed**	0	1	Passed	Passed
N4790_1	Passed	**Failed**	0	1	Passed	Passed
N4790_2	Passed	**Failed**	0	1	Passed	Passed
N4790_3	Passed	Passed	0	0	Passed	Passed
N4791_6	Passed	**Failed**	0	1	Passed	Passed
N4791_7	Passed	**Failed**	1	0	Passed	Passed
N4791_8	Passed	Passed	0	1	Passed	Passed
N4791_9	Passed	Passed	0	0	Passed	Passed
N4791_18	Passed	Passed	0	0	Passed	Passed
N4791_19	Passed	Passed	0	0	Passed	Passed
N4790_20	Passed	**Failed**	0	1	Passed	Passed
N4790_21	Passed	**Failed**	0	1	Passed	Passed
N4790_13	Passed	Passed	0	0	Passed	Passed
N4790_14	Passed	**Failed**	1	0	Passed	Passed
N4790_15	Passed	Passed	0	0	Passed	Passed

one – the same sensors fails the grading. However, the result at CERN off dicing frame are much worse. Surprisingly, one sensor that failed before, is marked as good in this configuration. Another 8 out of 15 previously good sensors fail the requirement on total current increase between 600 V and 800 V. The number of bad cells is also higher.

The presented results show that the process of removing the sensors from the dicing frame significantly worsen their properties. The sensors may sustain some mechanical damages during this activity. The effect is especially visible in the guard ring current, which grows notably high. Many of the sensors fail the grading. Therefore, the procedure of removing the sensors from the dicing frame at CERN should be improved or should be performed at Hamamatsu.

The second measurement performed during the electrical characterisation of the full sensor is capacitance (CV) measurement. This property, similarly as the IV, is measured as a function of the bias voltage. The sensors are also graded in terms of properties obtained from the CV measurement. The requirements in this case are as follows:

- depletion voltage median is less than 370 V for sensor of assumed thickness of 300 µm,
- interquartile range between 16th and 84th percentiles of the data ($IQR_{68\%}$) is less than 10% of depletion voltage median,
- relative thickness variation is less than 10 µm.

An example of CV grading result for one sensor is shown in figure 6.13.

- Sensor has been graded with checksCollectionID 1.
- Global characteristics using FULL cells only:
  - Full depletion voltage V_{dep} = 281.2 V calculated as the median of depletion voltages across cells, after removing outliers outside quantile 16-84%.
  - V_{dep} < 370 V for sensor of **assumed thickness** of 300 μm: Passed
  - Variation across sensor ΔV_{dep} = 0.4 %
  - ΔV_{dep} <= Maximum variation across sensor of ± 10% for sensor of V_{dep} = 281.2 V: Passed
- Per-pad characteristics using FULL cells only:
  - C_{meas_mean} = 44.479 pF, computed as the measured open corrected serial capacitance averaged over cells
  - C_{bulk} = 43.307 pF, computed as $\epsilon_0 \cdot \epsilon_r \cdot A/thickness$, with A = 1.254 cm^2
  - Interpad capacitance C_{int} = (C_{meas_mean} - C_{bulk})/$perimeter$ = 0.281 pF/cm, with perimeter = 4.167 cm
  - C_{int} < 1.5 pF at V_{dep} + 50V at RT, measured at 1MHz: Passed (no criteria for the overall grading)
- Thickness uniformity across sensor using FULL cells only:
  - Relative thickness variation $\Delta thickness$ = 0.4 % < 10 / 300: Passed

Sensor has PASSED the requirements.

Figure 6.13: CV grading example for sensor N4791_6 measured at CERN on dicing frame [26].

To present the results of the CV measurement, the hexplots are also used. End capacitance across the sensor is presented in this type of plot, as shown in figure 6.14. Different capacitance values for cell with different geometries can be observed. For the standard cells, the end capacitance value at bias voltage of 400 V is around 45 pF. The capacitance as a function of the bias voltage for all channels is shown in figure 6.15. Particular cells types are depicted in the legend. It is clearly seen that within one type of cell the CV curves are the same. By transforming this plot to inverse capacitance squared ($1/C^2$) as a function of the bias voltage, one can extract depletion voltage. The obtained values are present as hexplot, as shown in figure 6.16. For the first example

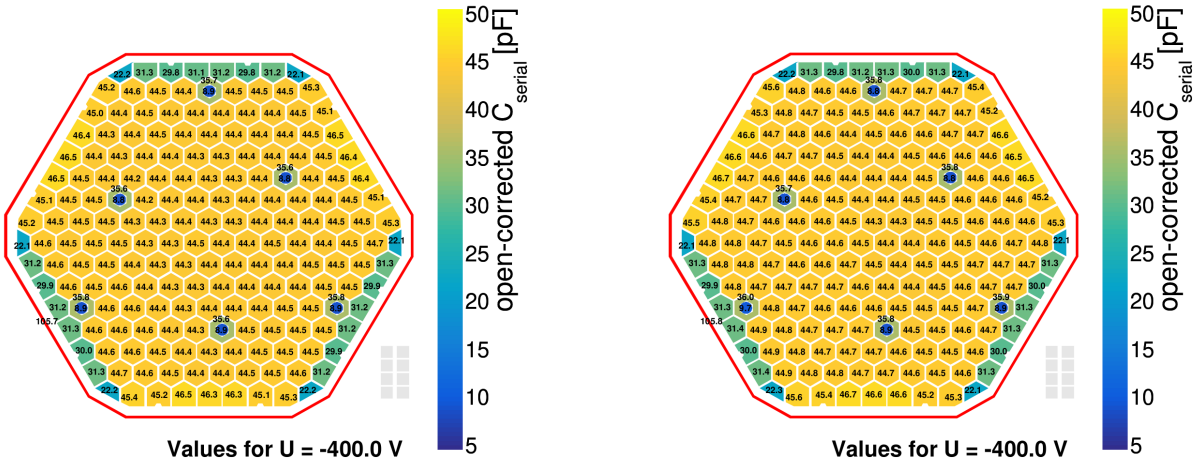

(a) Sensor ID: N4791_6 (b) Sensor ID: N4790_3

Figure 6.14: Exemplary hexplots showing end capacitance values at bias voltage of 400 V for two sensors [26].

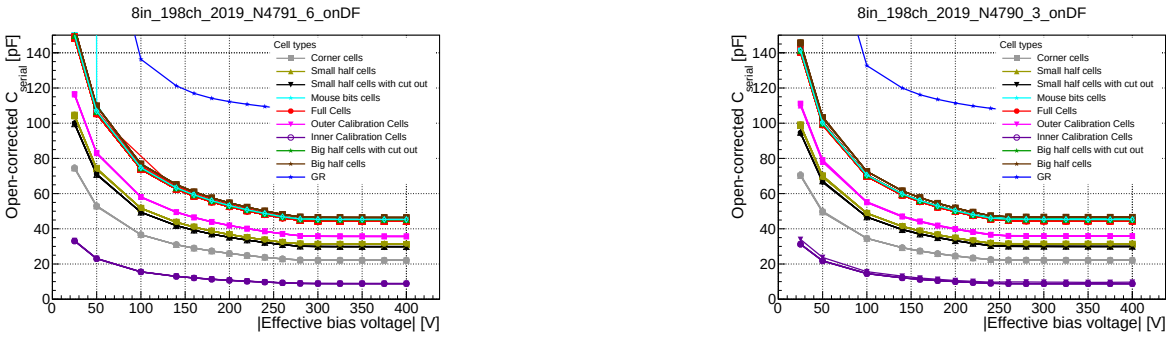

(a) Sensor ID: N4791_6 (b) Sensor ID: N4790_3

Figure 6.15: Exemplary plots showing CV curves for all channels of two sensors [26].

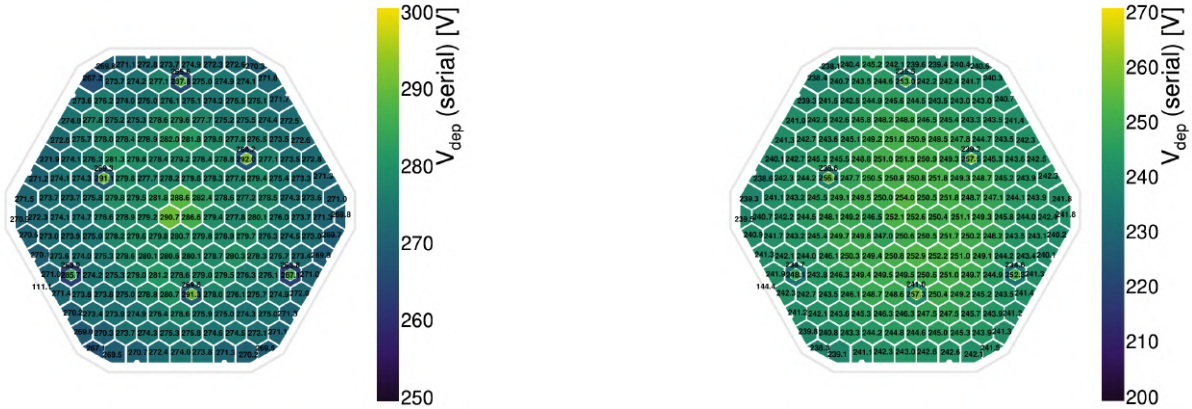

(a) Sensor ID: N4791_6 (b) Sensor ID: N4790_3

Figure 6.16: Exemplary hexplots showing depletion voltages for two sensors [26].

(fig. 6.16a, oxide type C) a spread of the depletion voltage value ranges between 265 V and 290 V, where the lowest values are for outer calibration cells and edge cells and the highest for the inner calibration cells and central standard cells. For the second example

Table 6.4: CV grading results of the sensors measured at CERN on dicing frame.

Sensor ID	V_{dep} corresponding to thickness	Maximum variation of V_{dep} across sensor of ± 10%	Thickness variation < 10 µm
N4791_1	Passed: 284.9V<370V	Passed: 0.9%	Passed: 2.4 um
N4791_2	Passed: 290.3V<370V	Passed: 0.7%	Passed: 2.4 um
N4790_1	Passed: 262.7V<370V	Passed: 1.2%	Passed: 1.2 um
N4790_2	Passed: 267.7V<370V	Passed: 1.1%	Passed: 1.2 um
N4790_3	Passed: 251.0V<370V	Passed: 0.9%	Passed: 1.8 um
N4791_6	Passed: 281.2V<370V	Passed: 0.4%	Passed: 1.2 um
N4791_7	Passed: 282.3V<370V	Passed: 0.3%	Passed: 0.9 um
N4791_8	Passed: 283.0V<370V	Passed: 0.4%	Passed: 1.5 um
N4791_9	Passed: 283.5V<370V	Passed: 0.4%	Passed: 1.2 um
N4790_13	Passed: 271.3V<370V	Passed: 0.4%	Passed: 1.5 um
N4790_14	Passed: 269.8V<370V	Passed: 0.5%	Passed: 1.2 um
N4790_15	Passed: 266.8V<370V	Passed: 0.9%	Passed: 0.9 um

Table 6.5: CV grading results of the sensors measured at CERN off dicing frame.

Sensor ID	V_{dep} corresponding to thickness	Maximum variation of V_{dep} across sensor of ± 10%	Thickness variation < 10 µm
N4791_1	Passed: 285.8V<370V	Passed: 0.9%	Passed: 2.7 um
N4791_2	Passed: 293.1V<370V	Passed: 0.7%	Passed: 2.4 um
N4790_1	Passed: 261.8V<370V	Passed: 1.2%	Passed: 1.2 um
N4790_2	Passed: 267.6V<370V	Passed: 1.2%	Passed: 1.2 um
N4790_3	Passed: 251.2V<370V	Passed: 0.9%	Passed: 1.8 um
N4791_6	Passed: 282.7V<370V	Passed: 0.5%	Passed: 1.2 um
N4791_7	Passed: 281.6V<370V	Passed: 0.3%	Passed: 1.2 um
N4791_8	Passed: 283.0V<370V	Passed: 0.4%	Passed: 1.5 um
N4791_9	Passed: 283.0V<370V	Passed: 0.4%	Passed: 1.5 um
N4791_18	Passed: 281.1V<370V	Passed: 0.2%	Passed: 1.2 um
N4791_19	Passed: 281.2V<370V	Passed: 0.3%	Passed: 1.8 um
N4791_20	Passed: 281.5V<370V	Passed: 0.4%	Passed: 2.4 um
N4791_21	Passed: 276.2V<370V	Passed: 0.5%	Passed: 1.8 um
N4790_13	Passed: 271.0V<370V	Passed: 0.4%	Passed: 1.5 um
N4790_14	Passed: 269.6V<370V	Passed: 0.7%	Passed: 1.2 um
N4790_15	Passed: 267.4V<370V	Passed: 1.0%	Passed: 0.9 um

(fig. 6.16b, oxide type B) the scatter of values is in a different range, between 235 V and 255 V. Similarly as in the previous example, the lowest values are in the edges and outer calibration cells and the highest in the inner calibration cells and in the central part of the sensor. The difference in depletion voltage values can come from the fact that oxide layers were produced in different processes. Nevertheless, both results are acceptable.

Presented CV results examples are from the same sensors as for the IV exemplary results (fig 6.8, 6.9, 6.10). They exhibit very good capacitance properties and pass the grading.

In terms of the CV measurement, the results from CERN before and after dicing frame removal are compared as Hamamatsu do not measure the capacitance for all channels. To summarize these results, the grading tables are presented – table 6.4 for CERN on dicing frame and table 6.5 for CERN off dicing frame. In both cases all the tested sensors passed the CV grading. The results are consistent before and after dicing frame removal. Noteworthy is the fact that there is a difference in depletion voltage values between oxide types. For the oxide A the value is around 290 V, for the oxide B – around 260 V, for the oxide C – around 280 V and for the oxide D – around 270 V. All of these results are acceptable, as they are lower than 370 V. The variation of the depletion voltage value is generally small and do not exceed 1.2%. Thickness variation across the sensors is well below 10 µm for all samples.

Chapter 7

Integration of IV/CV and TCT+ setups

7.1 Development strategy for the new setup

Up to the time of the thesis project, the leakage current and capacitance measurement (IV/CV, cf. sec. 5.1.1) and transient current technique (TCT) measurement (cf. sec. 5.1.2) of the silicon diodes were performed with 2 different setups. By performing these measurements, one can describe the radiation damage with 3 quantities – leakage current, capacitance and charge collection efficiency (CCE). By combining the two setups – creating a new IV/CV - TCT+ setup, faster turnaround can be achieved. Moreover, this approach can lead to better consistency between conducted measurements, as the measurement conditions (temperature, humidity) would be identical between the three measurements.

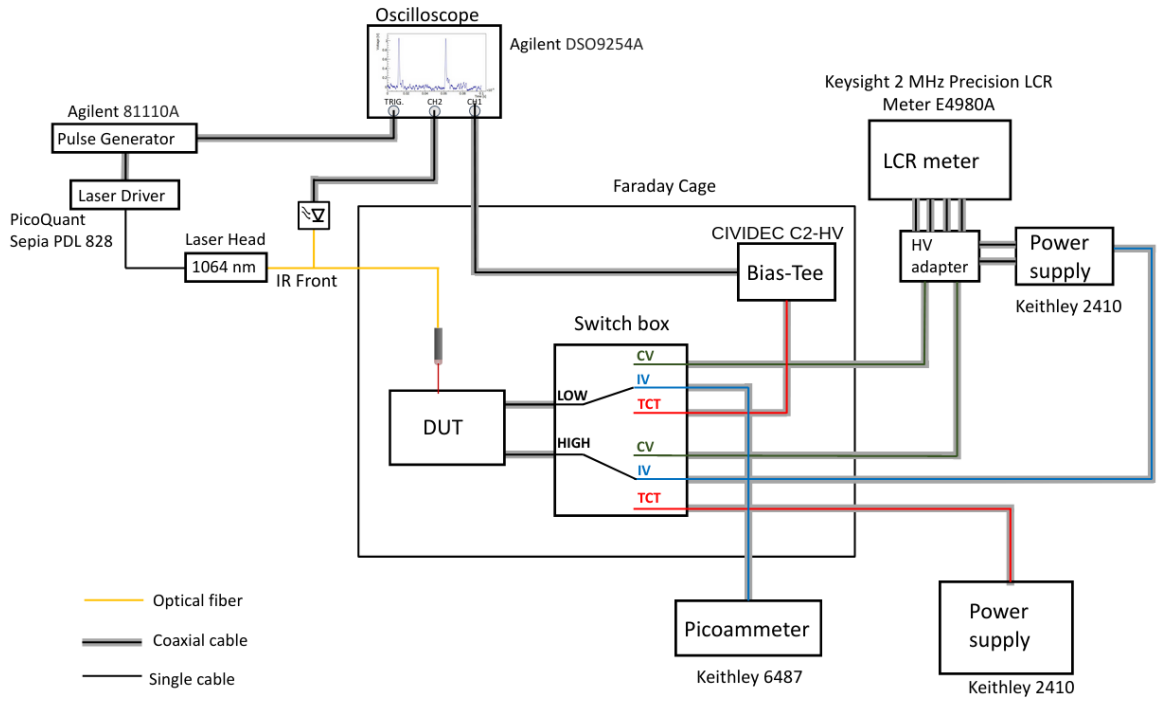

Figure 7.1: New setup diagram developed in this thesis, combining the IV/CV and TCT+ setups.

The strategy for the considered setup was to add a new IV/CV part to the existing TCT+ setup. The two setups are connected through a high frequency switch, which is a crucial element in the project. The detailed description of the switch is provided in the section 5.1. For the TCT measurements, where fast laser pulses are used, the high frequency of the switch is essential to obtain reliable results. The additional switch channels are added to conduct TCT measurements. The overview of the development strategy of the setup is shown in figure 7.1. The switch box is placed inside the Faraday cage, to keep it in a safe environment and also for logistic reasons, as it connects to the terminals of the DUT. Then, the switches' inputs are connected to the respective instruments (as shown in fig. 7.1). All of them are placed outside the Faraday cage, except for the amplifier (CIVIDEC) used for the TCT measurement.

In the TCT+ setup, there are 4 possible options for the measurement:

1) sensor biasing (HV) from the front side of the DUT and signal read from the back side of the DUT,

2) sensor biasing (HV) from the back and signal read from the front,

3) sensor biasing (HV) and signal read from the front,

4) sensor biasing (HV) and signal read from the back.

The presented diagram shows the setup ready to measure for option 1) and 2). For the remaining two options, another connection of the cables is needed. This will be discussed in detail in the section 7.3.

7.2 Assembling and testing the setup

7.2.1 Building IV/CV part of the setup

A new IV/CV setup was built (fig. 7.2), based on the concept of the existing one (cf. sec. 5.1.1). Then, the setup was commissioned by performing a set of test measurements as follows. All test results are compared to the reference measurement conducted in the original IV/CV setup.

A first test was performed by doing manual IV and CV scans (denoted in the following plots as "manual scan") for several voltage points as shown in fig. 7.3. The measurement temperature was room temperature, but not controlled. High observed leakage current results came from insufficient light blocking from the sample. Moreover, a decoupling box failure was found during the test. A scan was taken using another, functional, box (borrowed from the other setup). Otherwise, the test was successful and showed that the setup is working properly and gives reasonable results.

A second manual CV scan was performed, when the original decoupling box was repaired. The offset in the end capacitance between original measurement and this test (visible in fig. 7.3) comes from the difference in determining the open-correction value and it's precision. For the manual scan, the open-correction value was set to 50 pF, while the value was 49.4 pF for the automatic scan. Depletion voltages are in agreement to the reference measurement. This test was considered as successful, the setup gives reasonable results with the original decoupling box.

The next three tests were performed with the use of an automatic scanning software as shown in fig. 7.3. The obtained leakage current results were too high because of insufficient

light blocking. The following 2 tests showed that the leakage current decreased, when the amount of light within the area of DUT was minimised and the results are comparable to the original measurement. All CV test measurements are also in agreement with the reference measurement. The tests were satisfying, they shown that the setup can be run with the software.

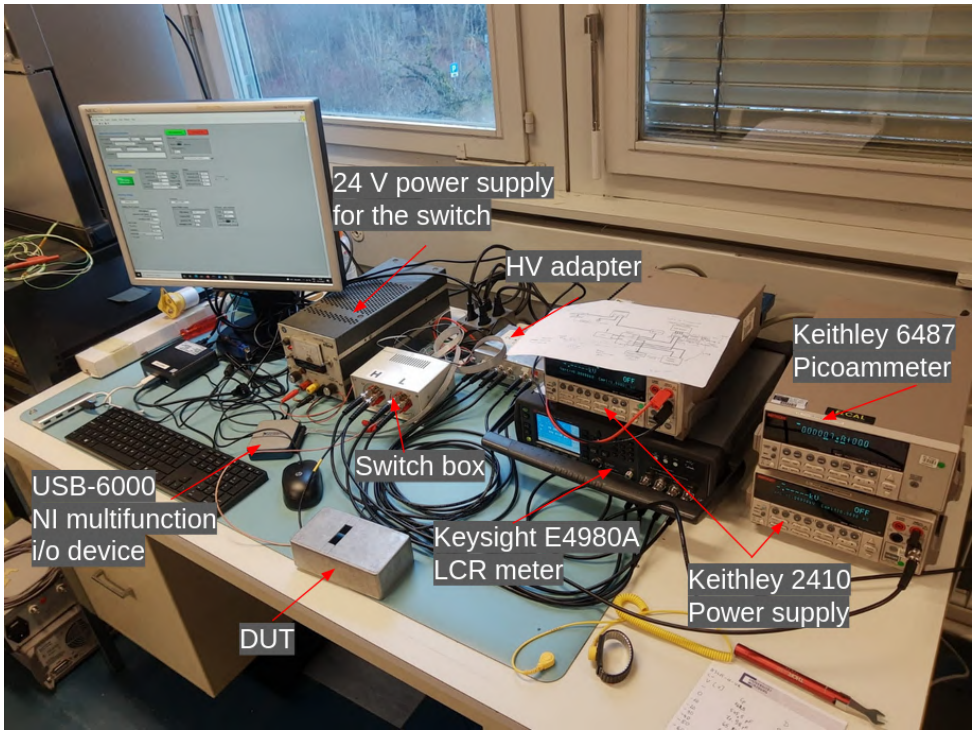

Figure 7.2: First assembly of the instruments for the new IV/CV setup as a part of the combined IV/CV - TCT+ setup.

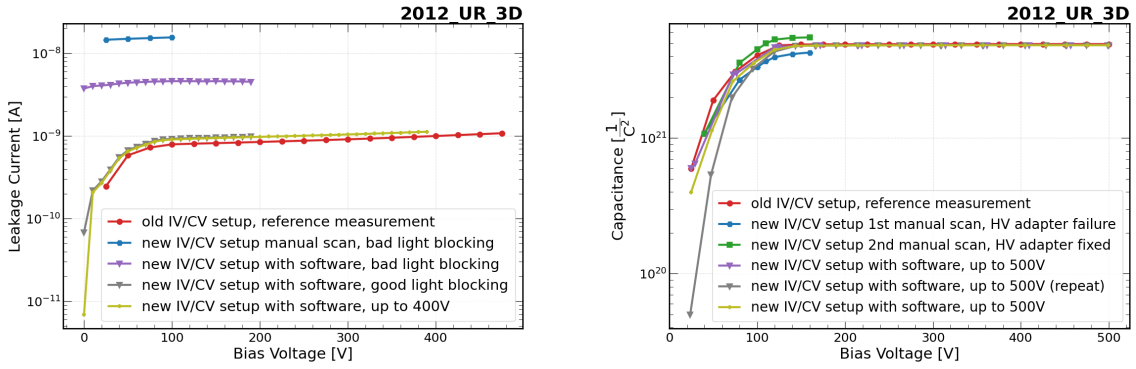

(a) (b)

Figure 7.3: (a) IV and (b) CV (inverse-squared capacitance as a function of bias voltage) first test measurements.

7.2.2 Validation of switch usability in the TCT+ setup

A high frequency switch had never been used before in this thesis work in the TCT+ setup, therefore its impact on the noise level as well as signal shape and amplitude needed

to be examined. In order to perform this test, the amplifier had to be exceptionally placed outside the Faraday cage (fig. 7.4). To correctly interpret the results, first the impact of putting the amplifier outside the Faraday cage was checked. Only then the switch was connected and tested. Two tests were conducted – the first with an n-type diode, the second with an low gain avalanche detector (LGAD), both differ in their noise level. The LGAD has a much lower noise level than the n-type diode.

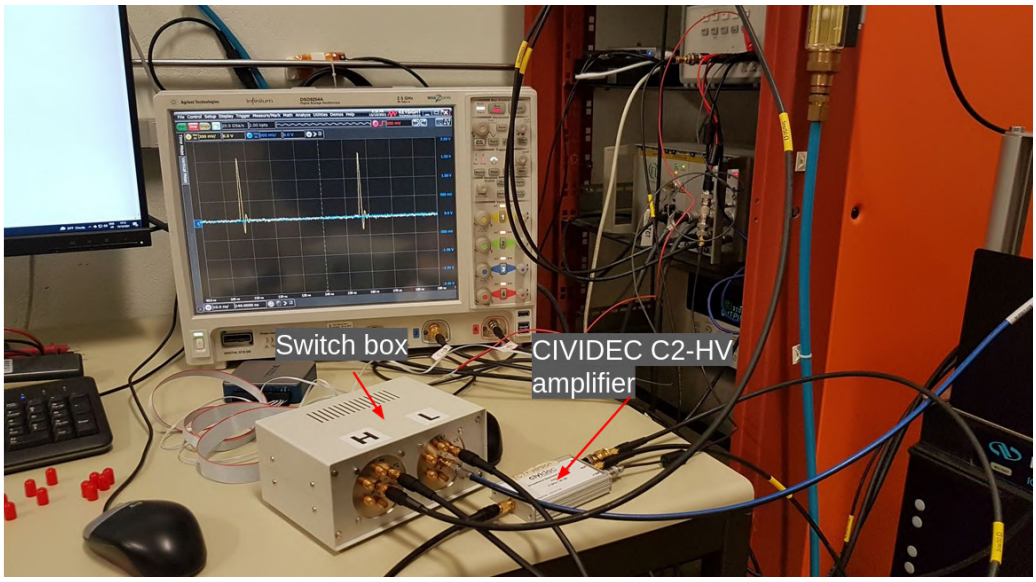

Figure 7.4: Test of the switch impact in the TCT+ setup.

Figures 7.5 and 7.6 show a histogram of the signal baseline, acquired for the first 10 ns of each trigger (no averaging was used for obtaining the signal). The histogram was fitted with a Gaussian fit. The noise level is defined as the sigma value obtained from the Gaussian fit.

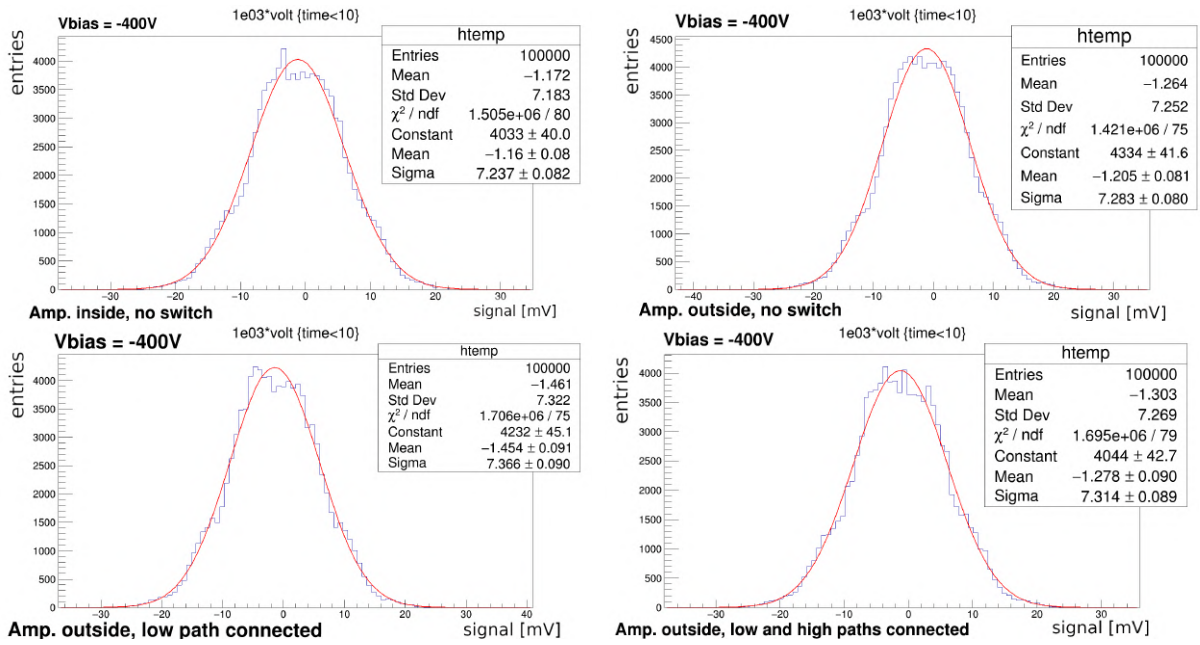

Figure 7.5: Noise level testing for the n-type diode.

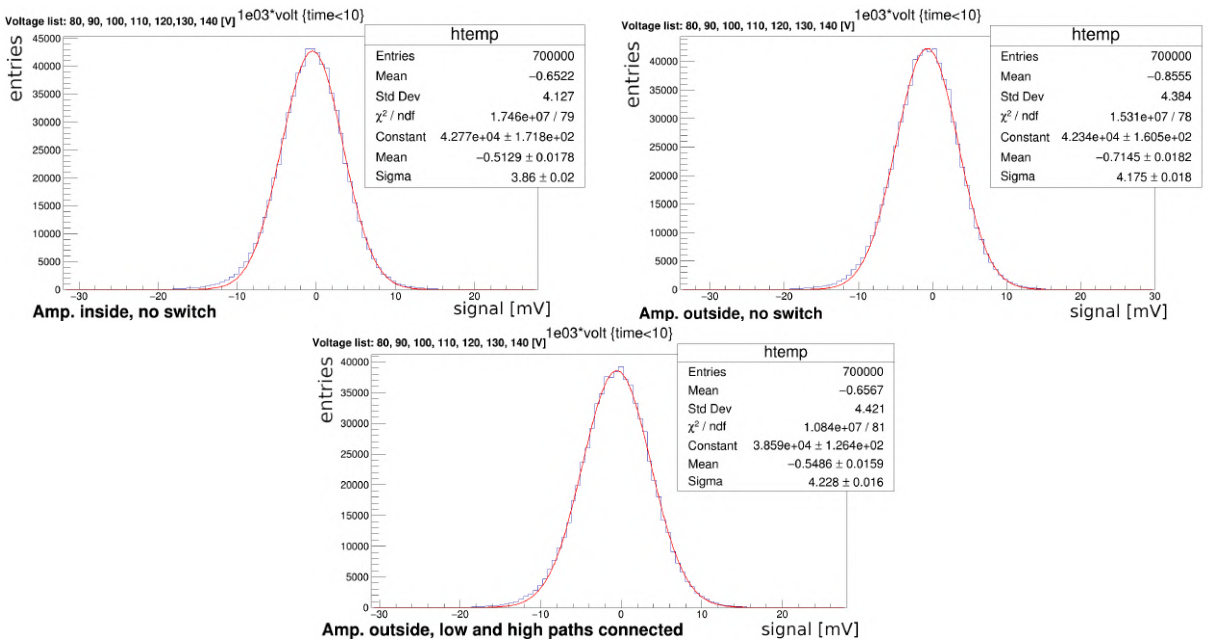

Figure 7.6: Noise level testing for the LGAD.

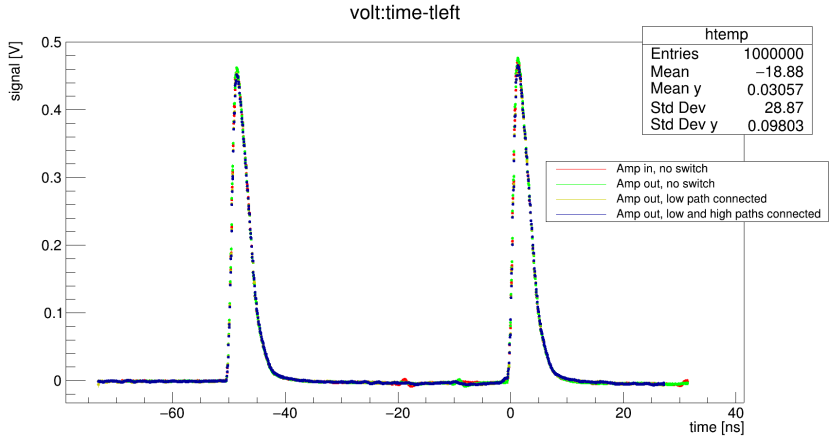

Figure 7.7: Profile histogram of a TCT signal for the n-type diode.

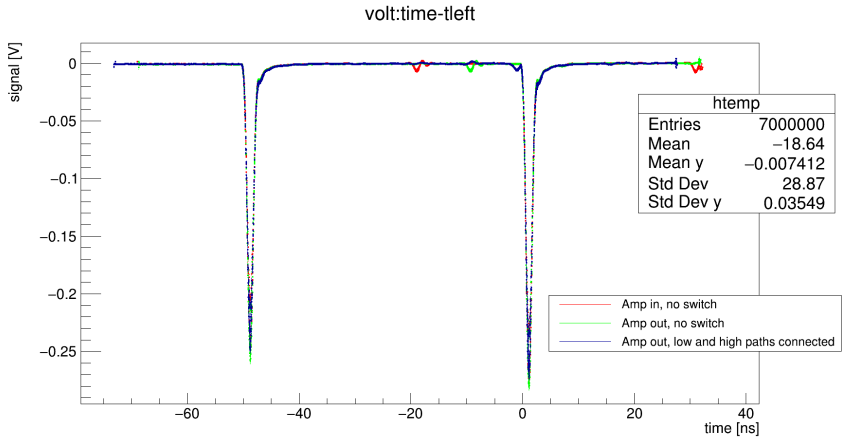

Figure 7.8: Profile histogram of a TCT signal for LGAD.

The table 7.1 summarises all measurements results (sigma values from the Gaussian fits) done in this check. The n-type diode (FZ320N) has a noise level of around 7.2 mV. After change of the amplifier location and adding the switch, the noise level slightly increases to around 7.3 - 7.35 mV, corresponding to ∼2%. For the LGAD, which has much lower noise level (of around 3.86 mV), it increases by 0.3 mV when the amplifier is put outside, corresponding to ∼10%. However, adding the switch does not raise the noise level significantly (less than 1.5%). It is clear that in this case, the noise level is increased by change of the amplifier location. In summary, adding the switch into the signal path does not have a significant impact on the noise level.

Table 7.1: Noise levels for each test structure and for all configurations.

	Sigma (from the fit) [mV]			
Test structure	Amplifier inside	Amplifier outside	Switch low	Switch high
FZ320N	7.237	7.283	7.366	7.314
LGAD	3.86	4.175	–	4.228

Besides that, the signal shape was examined. The results shown in figures 7.7 and 7.8 prove that the switch also does not have a significant impact on the signal shape.

7.2.3 Installing the IV/CV setup in the TCT lab

After validation of the new IV/CV setup (cf. section 7.2.1), it could be moved to the TCT+ lab. It required some adaptation of the TCT+ lab – for instance adding an additional shelf in the rack for the instruments and mounting new SMA connectors to the Faraday cage wall.

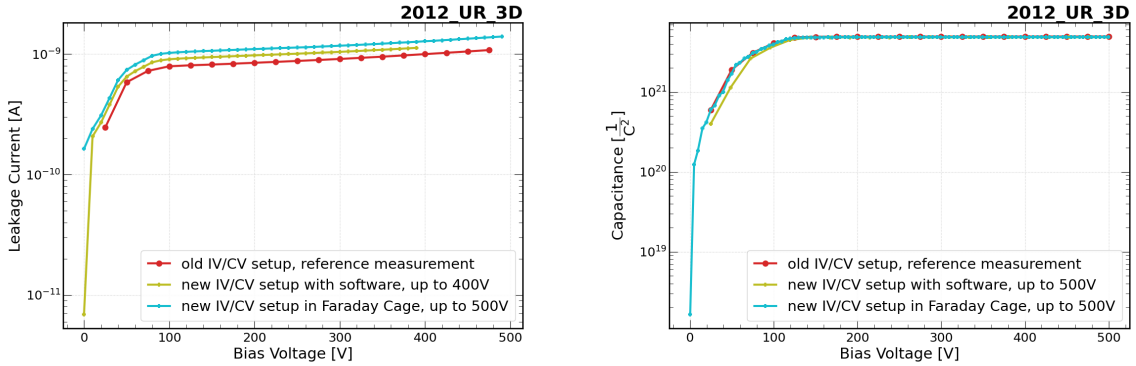

(a) (b)

Figure 7.9: (a) IV and (b) CV test measurement results after installing the IV/CV setup in the TCT+ lab compared to the reference measurement.

As a first step, the IV/CV setup was connected separately from the TCT+ setup and its functionality was cross-checked. At this stage the temperature during the measurement was not controlled yet. Results of the IV and CV test measurements are shown in figure 7.9. The results are in agreement with previously taken reference measurements.

Then, a third channel in the switch was activated. For this, changes in the binary coding of the switch and connections to the multifunction device had to be made. For the separate connection of all channels (as it is done in IV/CV setup, cf. fig. 5.3), 6 outputs would be needed (2 per each type of measurement). Since the multifunction device has only 4 outputs, the high and low paths for each type of measurement are now connected together and put to the same output (fig. 7.10). This results in the new switch binary coding in the software:

- CV: 0001,
- IV: 0010,
- TCT: 0100.

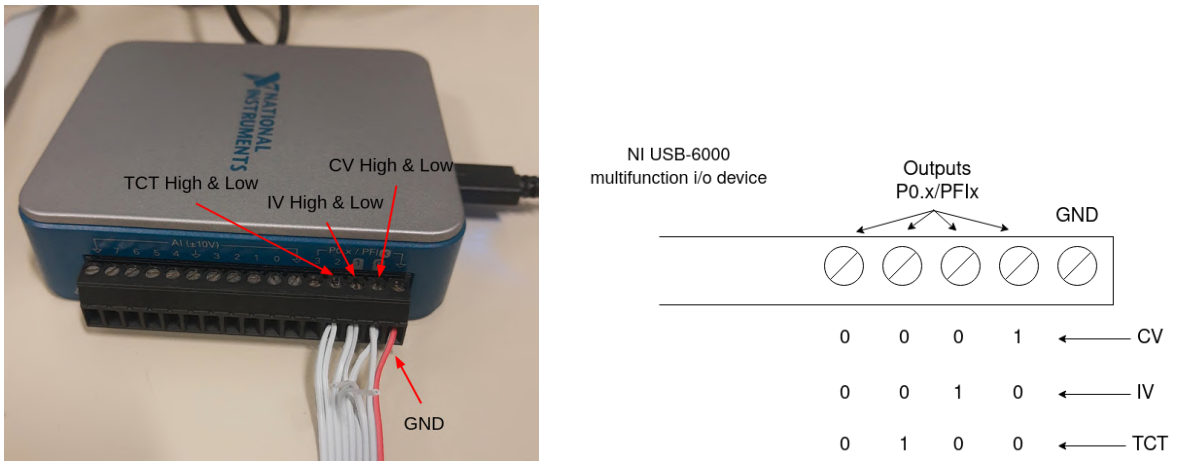

(a) (b)

Figure 7.10: Connections of the switch channels to the NI multifunction device in the IV/CV - TCT+ setup.

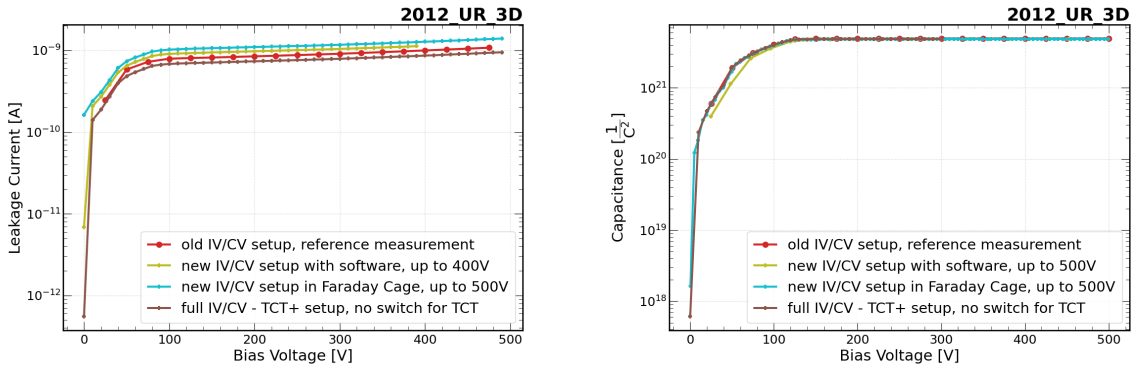

(a) (b)

Figure 7.11: Comparing (a) IV and (b) CV test measurements including test on the full IV/CV - TCT+ setup.

After adding the TCT channel to the switch, all cable connections were done and the full IV/CV - TCT+ setup was tested. Two softwares are used for controlling the

measurement – the existing TCT and IVCV Labview programs. The temperature was controlled by the TCT software. Changing to the TCT channel in the switch was done manually, as this is not implemented yet in the software. For comparison of IV and CV results, only selected measurements are shown (fig. 7.11). The tests measurements are in agreement to the previous measurements, the slight difference in the leakage current comes from the temperature difference.

The last step was to adapt the softwares for the new setup. The essential updates were: changing the switch binary code, adding the third channel for the TCT measurement and enabling the IVCV software to read the temperature from the TCT software (from which the temperature is controlled). The full IV/CV - TCT+ setup is controlled by two mentioned programs running simultaneously. By default, the IVCV software sets the channel 3 in the switch, which is the TCT measurement.

7.3 Commissioning the setup

Pictures of the full setup are presented in fig. 7.14. The final test of the combined IV/CV - TCT+ setup was performed. Crosschecks with the IV/CV setup were also performed as shown in fig. 7.12. A small difference in the leakage current comes from a slight difference in measurement temperature between the probe stations. CV measurements show the same depletion voltage, end capacitance and curve shape. TCT test measurement with

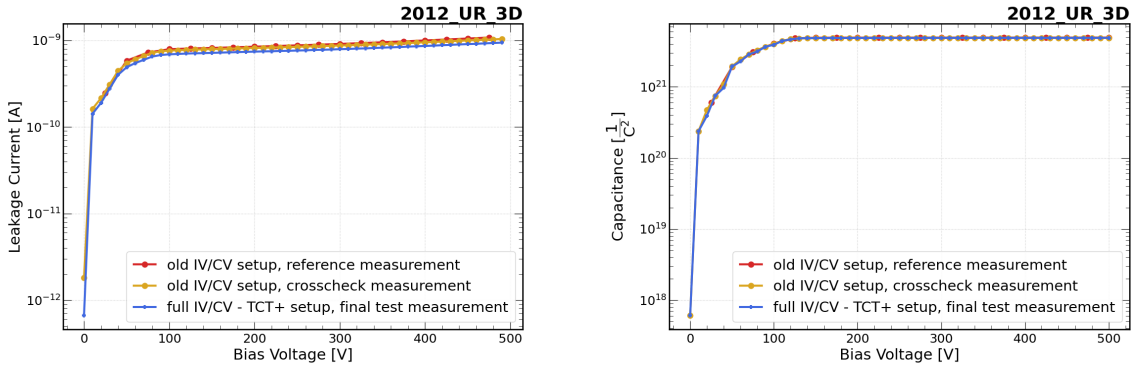

(a) (b)

Figure 7.12: (a) IV and CV (b) final test measurements.

the considered setup is presented in fig. 7.13. The signal shape is compatible with the signal shape obtained using the original SSD TCT setup.

As mentioned in the section 7.1, depending on the selected configuration of the TCT measurement, different connections of the cables will be applied. There are 4 possible options of the measurement presented as two configurations:

1. Sensor biasing (HV) from the front side of the DUT and signal read from the back side of the DUT **or** sensor biasing (HV) from the back and signal read from the front.

2. Sensor biasing (HV) and signal read from the front **or** sensor biasing (HV) and signal read from the back.

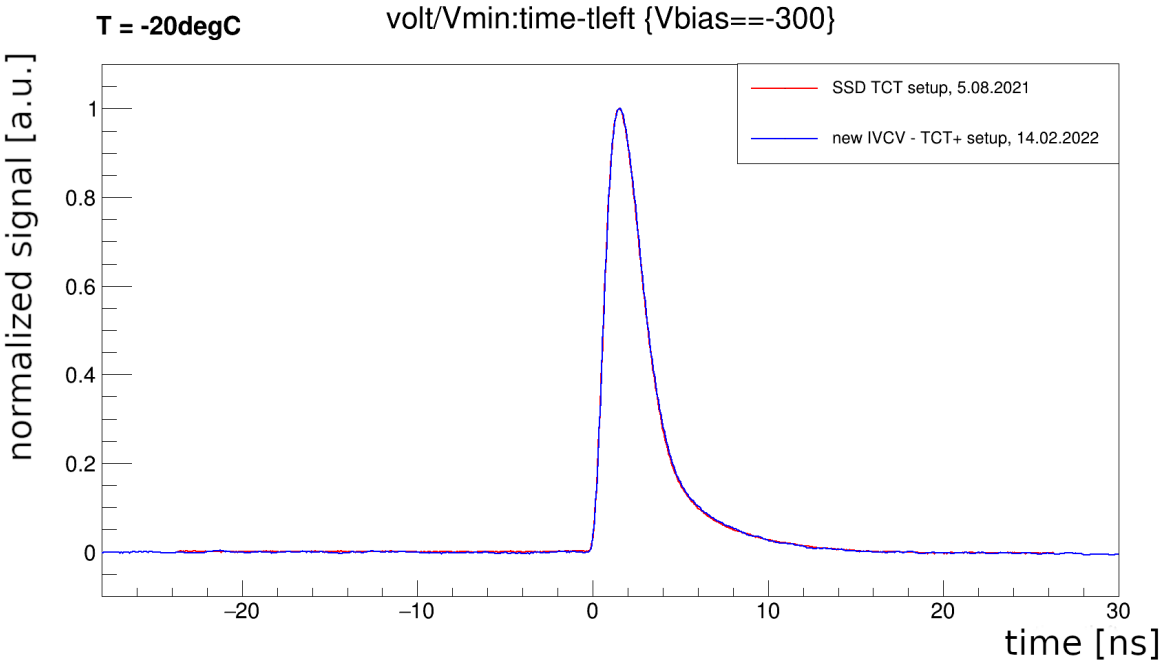

Figure 7.13: TCT final test measurement on the full IV/CV - TCT+ setup compared to the reference measurement performed on the original SSD TCT setup. Both curves are normalized to the signal amplitude.

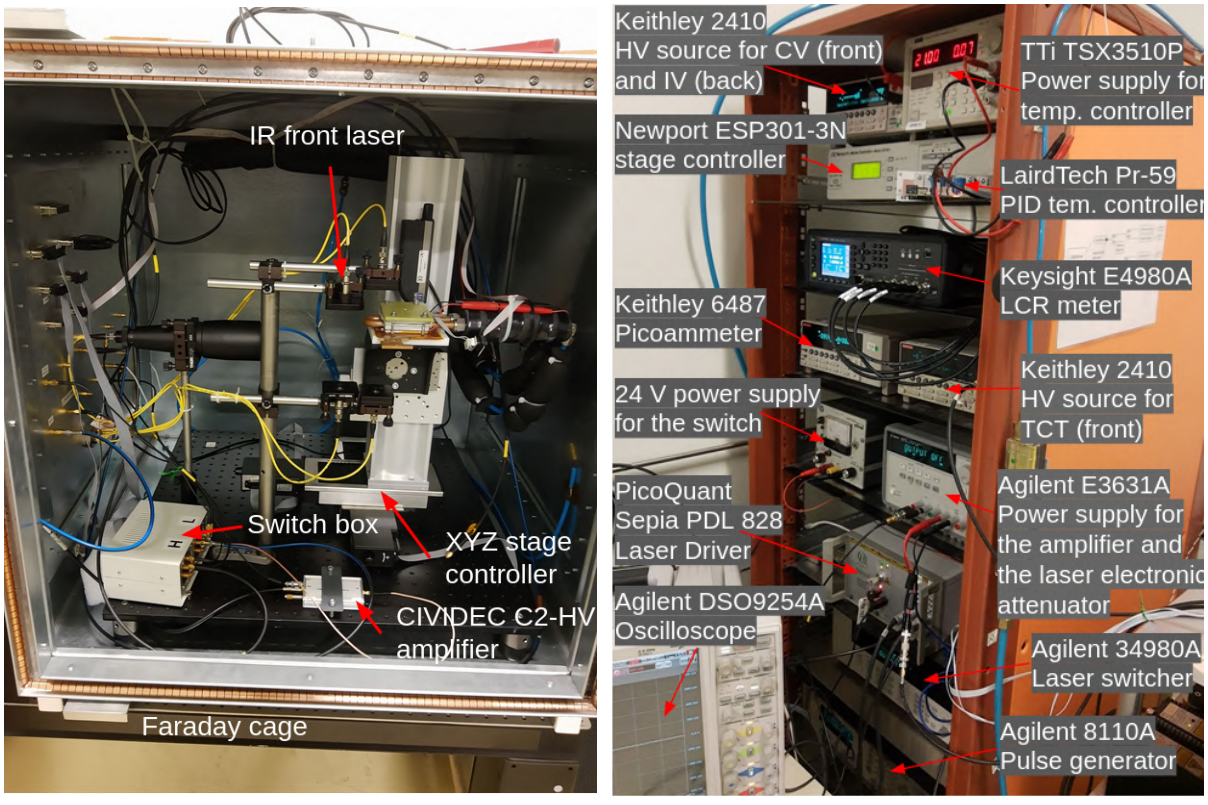

(a) (b)

Figure 7.14: Pictures of the full IV/CV - TCT+ setup, (a) view inside the Faraday cage and (b) the instruments.

Each configuration has two options depending on the desired polarity of the measurement. However, the only difference is in connecting the DUT. Therefore these two options are considered the same and described together in terms of preparation of the measurement and cable connection. The user has to choose the polarity and connect the DUT respectively.

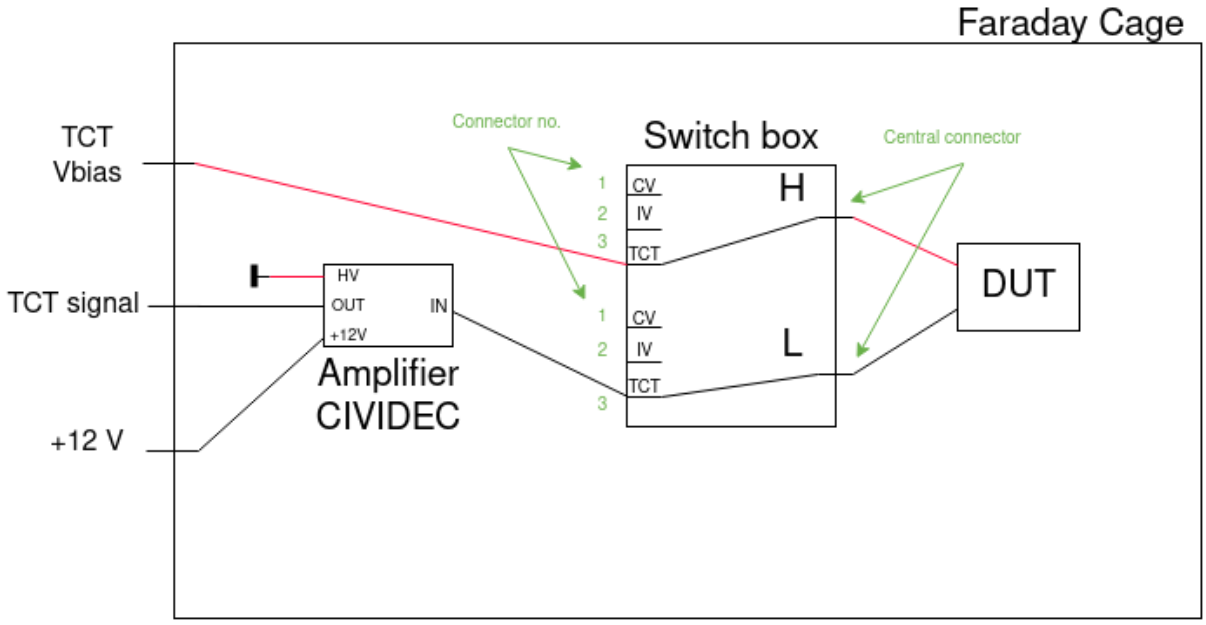

Figure 7.15: Diagram of cable connections for configuration 1.

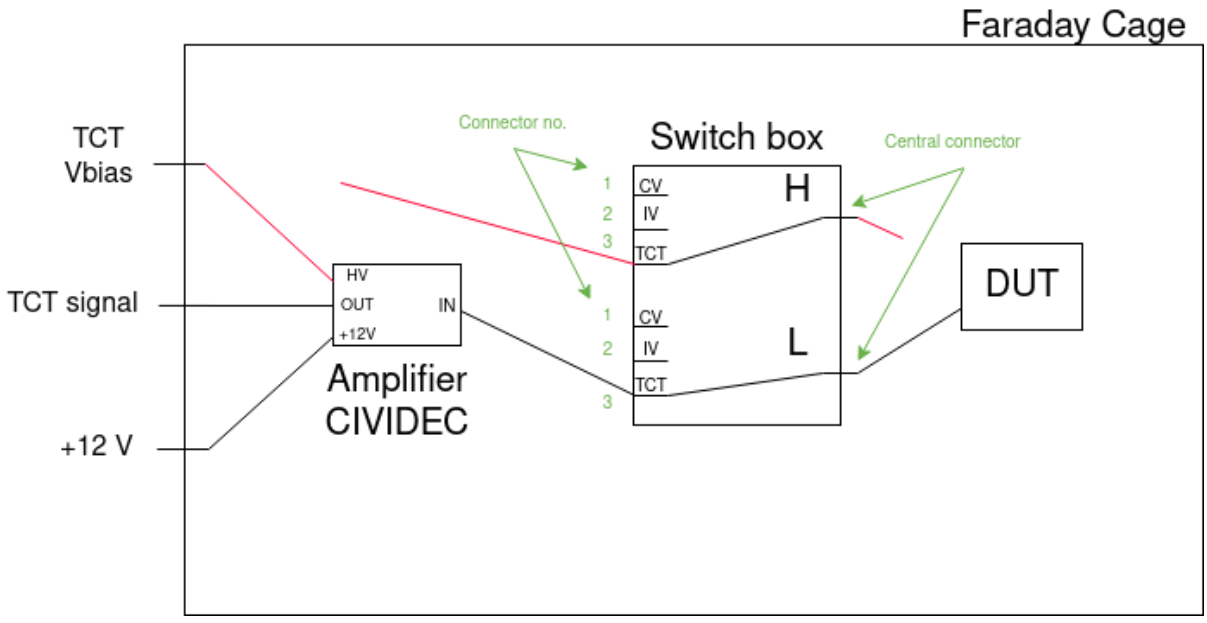

Figure 7.16: Diagram of cable connections for configuration 2.

In configuration 1. (fig. 7.15), the sensor biasing and signal read is performed by two separate cables. The signal line goes from the DUT to the central connector of the low path of the switch (cf. fig. 5.2, right side). Then, the line goes from connector no. 3 to the amplifier input ("IN"). Finally, from the amplifier output ("OUT") the cable is connected to the "signal" connector located in the Faraday cage wall, which connects to

the oscilloscope. The HV line goes from the DUT to the central connector of the high path of the switch. Then, the line goes from connector no. 3 to the "sensor bias" connector in the Faraday cage wall. The high voltage output in the amplifier ("HV") is terminated (by a coaxial cable and 50 Ω termination). In this configuration, the user can automatically perform TCT, IV and CV measurements, as no changes in the cabling is required and the switch is operated by the software.

The configuration 2. (fig. 7.16) is meant for the TCT measurements where sensor biasing and signal reading is performed on the same side of the DUT. Therefore, only one cable is used to connect the DUT. It is the signal cable that, similarly as in the first configuration, goes to the central connector of the low path of the switch. Then, the line goes from the connector no. 3 to the amplifier input. From the amplifier output the cable is connected to the "signal" connector located in the Faraday cage wall. The high voltage output is connected to the "sensor bias" connector in the Faraday cage wall. The high path of the switch is not used. The high side of the PCB of the DUT should be terminated. This configuration allows only for the TCT measurement.

The setup is organised in such a way that enables effortlessly to change between the configurations. The lines marked in red in figures 7.15 and 7.16 indicate the cables that have to be rearranged in order to change the configuration. The connectors of the switch box should be untouched, as they are difficult to access. To change from the configuration 1. to configuration 2., the cable from the "sensor bias" connector has to be detached. Then, the termination of the high voltage output in the amplifier should be detached. Finally, the remaining cable from the high voltage output should be connected to the "sensor bias" connector. To change from the configuration 2. to configuration 1., the cable from the "sensor bias" connector has to be detached. Then, to this cable a 50 Ω termination has to be attached. Finally, the cable from the channel 3 of the box should be connected to the "sensor bias" connector.

7.4 Conclusions

In summary, a new setup was created by assembling a new IV/CV setup and combining with the existing TCT+ setup. The results obtained with the new combined setup are consistent with reference measurements. The new setup still needs a few upgrades. For example, the compatibility of the IV and CV results at low temperatures has to be validated (only the TCT measurement was performed at -20°C, c.f. fig. 7.13). Moreover, the software could be combined in one so that it would be easier to use. However, the setup is in a functional state, i.e. it is ready to be used for measurement campaigns of the silicon diodes and other devices of similar size.

Chapter 8

Summary

The present thesis is devoted to silicon sensor characterisation and radiation hardness qualification for the CMS Endcap Calorimeter Upgrade. The project is part of the High-Luminosity LHC program. The current Endcap Calorimeter will be replaced by the High Granularity Calorimeter. HGCAL is a sampling calorimeter and will be based on silicon sensors as active material in high radiation regions. The silicon sensors are produced in hexagonal geometry diced from 8-inch wafers. On the remaining pieces of the wafers, test structures are produced. During the time of the thesis work, several activities were performed. They include the electrical characterisation and charge collection study of the test structures, electrical characterisation of full hexagonal sensors and integration of two initially separate setups for characterisation of the test structures.

The electrical characterisation of the test structures were performed on samples that were neutron irradiated at the two institutes: JSI and RINSC and including an isothermal annealing study. The leakage current is decreasing with the annealing time. The beneficial part of the annealing where the depletion voltage was decreasing and the reverse part where the depletion voltage was increasing were clearly seen. The comparison of the electrical properties showed a discrepancy of the fluence estimation between JSI and RINSC institutes. As the JSI is well established irradiation site, it was concluded the fluence estimation at RINSC was not yet satisfactory and could be corrected.

The charge collection study of the test structures was performed on samples of different thicknesses and fluences. The results of the measurements showed that the efficiency of the charge collection is decreasing with the fluence. Moreover, the thinner the diode, the higher the charge collection efficiency. Several steps of the annealing were also performed. It was observed, that charge collection efficiency does not change significantly with annealing time for any thickness. This type of measurement could be done only on the test structures, as up to the time of the thesis project, there is no functional setup for the charge collection study for the full sensors.

The electrical characterisation of the full sensors was performed only on the unirradiated samples. They were measured in three configurations: at the producer (HPK), at CERN on dicing frame and at CERN after removing from the dicing frame. After each measurement, the sensor is graded and classified as "passed" or "failed". The grading results for the samples measured at HPK and at CERN on dicing frame were good, as only 1 out of 16 sensor failed the grading. However, removing the sensors from the dicing frame significantly degraded their IV properties, as 8 out of 16 sensors failed the grading. The procedure of removing the sensors from the dicing frame at CERN should be improved or should be performed at HPK. All the tested sensors passed the CV grading,

both on and off the dicing frame. The further step in the electrical characterisation of the full sensors is to study the properties of the irradiated sensors. Currently, the 8-inch sensors can be irradiated only at RINSC due to their size. That is why the accuracy of the fluence estimation at RINSC should be well established.

The last activity presented in this thesis was the integration of the IVCV and TCT+ setups for the test structures. The motivation of the project was to achieve faster turnaround and better consistency between conducted measurements. The integration was successful, as the results obtained with the new combined setup are consistent with reference measurements, performed on the already existing setups. The setup is in a functional state, but still needs a few upgrades. For example the software, as there are two separate programs to control the measurement – one for the IVCV and one for the TCT. They should be integrated into one program. Moreover, no IV and CV measurements at low temperatures were performed up to the time of the thesis work.

In the next phase of the CMS Endcap Calorimeter Upgrade, the prototypes that show the best performance will be chosen and the producer will start the mass production of the sensors. In total, CMS HGCAL will contain about 3000 8-inch silicon sensors. With this thesis work, the understanding of the silicon sensors prototypes and their radiation tolerance were improved. Lessons learned will be applied in the upcoming production rounds.

Bibliography

[1] C. Fabjan et al., *Technology meets research - 60 years of CERN technology: Selected highlights*. 04 2017.

[2] E. Mobs, "The CERN accelerator complex - 2019. Complexe des accélérateurs du CERN - 2019." http://cds.cern.ch/record/2684277, 2019. Last accessed: 30 November 2021.

[3] CERN, "The Standard Model." https://home.cern/science/physics/standard-model, 2022. Last accessed: 19 May 2022.

[4] CERN, "CERN's accelerator complex." https://home.cern/science/accelerators/accelerator-complex, 2022.

[5] CERN, "The Large Hadron Collider." https://home.cern/science/accelerators/large-hadron-collider, 2022. Last accessed: 19 May 2022.

[6] X. C. Vidal and R. C. Manzano, "Luminosity – Taking a closer look at LHC." https://www.lhc-closer.es/taking_a_closer_look_at_lhc/0.luminosity, 2022. Last accessed: 11 May 2022.

[7] O. Aberle et al., *High-Luminosity Large Hadron Collider (HL-LHC): Technical Design Report*. CERN Yellow Reports: Monographs, Geneva: CERN, 2020.

[8] CERN, "High-Luminosity LHC." https://home.cern/science/accelerators/high-luminosity-lhc, 2022. Last accessed: 19 May 2022.

[9] CERN, "New technologies for the High-Luminosity LHC." https://home.cern/new-technologies-high-luminosity-lhc, 2022. Last accessed: 19 May 2022.

[10] The CMS Experiment at CERN, "About CMS." https://cms.cern/detector. Last accessed: 19 May 2022.

[11] CMS Collaboration, "The CMS experiment at the CERN LHC," *JINST 3 (2008) S08004*, 2008.

[12] C. W. Fabjan and F. Gianotti, "Calorimetry for particle physics," *Reviews of Modern Physics*, vol. 75, 2003.

[13] V. Hinger, *Silicon Sensor Process Quality Control for the CMS Phase-2 Upgrade*. PhD thesis, TU Vien, 2021. http://cds.cern.ch/record/2766455.

[14] T. Quast, *Qualification, performance validation and fast generative modelling of beam test calorimeter prototypes for the CMS Calorimeter Endcap Upgrade*. PhD thesis, RWTH Aachen, 2020. http://cds.cern.ch/record/2746196.

[15] P. Paulitsch, "The Silicon Sensors for the High Granularity Calorimeter of CMS," *Nuclear Inst. and Methods in Physics Research, A*, vol. 978, 2020.

[16] Physics World, "CERN's new era for calorimeters." https://physicsworld.com/a/cerns-new-era-for-calorimeters/, 2021. Last accessed: 26 November 2021.

[17] CMS Collaboration, *The Phase-2 Upgrade of the CMS Endcap Calorimeter*. CERN-LHCC-2017-023 (CMS-TDR-019), 2017.

[18] D. Barney, "Overview slide of CE with main parameters." https://cms-docdb.cern.ch/cgi-bin/DocDB/ListBy?topicid=715. Last accessed: 24 November 2021.

[19] G. Lutz, *Semiconductor Radiation Detectors*. Berlin Heidelberg: Springer-Verlag, 2007.

[20] S. M. Sze and M. K. Lee, *Semiconductor Devices: Physics and Technology*. John Wiley & Sons, INC., 2012.

[21] F. Hartmann, *Evolution of Silicon Sensor Technology in Particle Physics*. STMP 231, Berlin Heidelberg: Springer, 2009.

[22] M. Moll, *Radiation Damage in Silicon Particle Detectors*. PhD thesis, Universität Hamburg, 1999. https://mmoll.web.cern.ch/thesis/pdf/moll-thesis.pdf.

[23] Photonics Laboratory, Korea University, "Basics of device fabrication." http://contents.kocw.or.kr/KOCW/document/2015/korea_sejong/youjonghoon/7.pdf. Last accessed: 25 November 2021.

[24] A. Junkes, *Influence of radiation induced defect clusters on silicon particle detectors*. PhD thesis, Universität Hamburg, 2011. https://inspirehep.net/literature/940715.

[25] T. Bergauer, "GDS Design for HPK for 8" sensor from 2018." https://cms-docdb.cern.ch/cgi-bin/DocDB/ListBy?topicid=717. Last accessed: 24 September 2021.

[26] T. Quast et al., "HGC Sensor IVCV Analysis." https://gitlab.cern.ch/CLICdp/HGCAL/lcd_hgcal_analysisworkflows, 2022. Last accessed: 27 April 2022.

[27] T. Bergauer, "Half moon dicing and Dicing Foil Removal." https://indico.cern.ch/event/1069270/contributions/4525427/attachments/2308351/3927531/20210914_DicingFoil%20Removal.pdf.

[28] D. Zontar, *Study of radiation damage in silicon detectors for high luminosity eriments at LHC*. PhD thesis, University of Ljubljana, 1998. https://inis.iaea.org/collection/NCLCollectionStore/_Public/40/018/40018416.pdf?r=1&r=1.

[29] V. Dimic, "Twenty years of operation of Ljubljana's Triga Mark II Reactor." https://inis.iaea.org/collection/NCLCollectionStore/_Public/40/018/40018416.pdf?r=1&r=1.

[30] Department of Nuclear Sciences and Applications, "Research Reactor Details - RINSC Rhode Island NSC." http://www-naweb.iaea.org/napc/physics/research_reactors/database/RR%20Data%20Base/datasets/report/United%20States%20of%20America%20%20Research%20Reactor%20Details%20-%20RINSC%20RHODE%20ISLAND%20NSC.htm. Last accessed: 14 April 2022.

[31] T. Quast et al., "Neutron Irradiation and Electrical Characterisation of the First 8" Silicon Pad Sensor Prototypes for the CMS Endcap Calorimeter Upgrade." Unpublished, 2022.

[32] P. Almeida. Personal communication.

[33] M. Moll, "Displacement Damage in Silicon Detectors for High Energy Physics," *IEEE Transactions on Nuclear Science*, vol. 65, no. 8, pp. 1561–1582, 2018.

[34] Charter Engineering, INC., "Datasheet: H3 - H6 series SP3T - SP6T DC - 26.5 GHz." https://www.ceiswitches.com/h6pdf.pdf. Last accessed: 2 March 2022.

[35] National Instruments, "Specifications USB-6000 8 AI (10 kS/s), 4 DIO USB Multifunction I Device." https://www.ni.com/pdf/manuals/374113c.pdf. Last accessed: 2 March 2022.

[36] National Instruments, "User guide NI USB-6000 USB Multifunction DAQ Device." https://www.ni.com/pdf/manuals/373921a.pdf. Last accessed: 2 March 2022.

[37] E. C. Rivera, *Advanced silicon sensors for future collider experiments*. PhD thesis, Universidad de Cantabria, 2017. http://cds.cern.ch/record/2291517.

[38] S. Ramo, "Currents Induced by Electron Motion," *Proceedings of the IRE*, vol. 27, no. 9, pp. 584–585, 1939.

[39] J. Kieseler et al., "Radiation tolerance study using test-structure diodes from 8-inch silicon sensors for CMS HGCAL." https://indico.cern.ch/event/1074989/contributions/4601991/attachments/2349553/4007323/20211119_RD_50_kieseler.pdf.

[40] CIVIDEC Instrumentation GmbH, "Datasheet: C2-HV Broadband Amplifier, 2 GHz, 40 dB." https://cividec.at/index.php?module=public_action.act_download_PIS&id=34. Last accessed: 11 March 2022.

[41] E. Brondolin et al., "ARRAY: An open source, modular and probe-card based system with integrated switching matrix for characterisation of large area silicon pad sensors," *Nuclear Inst. and Methods in Physics Research, A*, vol. 940, pp. 168–173, 2019.

[42] P. Almeida, "CVIVplotter." https://gitlab.cern.ch/pdiasdea/cvivplotter, 2022. Last accessed: 29 April 2022.

[43] J. Kieseler, "HGCalSi." https://github.com/jkiesele/HGCalSi, 2022. Last accessed: 29 April 2022.

[44] P. Almeida, "HGCAL TCT-CCE." https://gitlab.cern.ch/pdiasdea/hgcal_tct-cce, 2022. Last accessed: 27 April 2022.